The Astrophysical Journal, 922:167 (19pp), 2021 December 1 https://doi.org/10.3847/1538-4357/ac1e97

First HETDEX Spectroscopic Determinations of Lyα and UV Luminosity Functions at $z = 2$–3: Bridging a Gap between Faint AGNs and Bright Galaxies

Yechi Zhang[1,2], Masami Ouchi[1,3,4], Karl Gebhardt[5], Erin Mentuch Cooper[5], Chenxu Liu[5], Dustin Davis[5], Donghui Jeong[6,7], Daniel J. Farrow[8,9], Steven L. Finkelstein[5], Eric Gawiser[10], Gary J. Hill[5,11], Yuichi Harikane[1,12], Ryota Kakuma[1], Viviana Acquaviva[13,14], Caitlin M. Casey[5], Maximilian Fabricius[8,9], Ulrich Hopp[8,9], Matt J. Jarvis[15,16], Martin Landriau[17], Ken Mawatari[1,3], Shiro Mukae[1], Yoshiaki Ono[1], Nao Sakai[1], and Donald P. Schneider[6,7]
[1] Institute for Cosmic Ray Research, The University of Tokyo, 5-1-5 Kashiwanoha, Kashiwa, Chiba 277-8582, Japan; yczhang@icrr.u-tokyo.ac.jp
[2] Department of Astronomy, Graduate School of Science, the University of Tokyo, 7-3-1 Hongo, Bunkyo, Tokyo 113-0033, Japan
[3] National Astronomical Observatory of Japan, 2-21-1 Osawa, Mitaka, Tokyo 181-8588, Japan
[4] Kavli Institute for the Physics and Mathematics of the Universe (Kavli IPMU, WPI), The University of Tokyo, 5-1-5 Kashiwanoha, Kashiwa, Chiba, 277-8583, Japan
[5] Department of Astronomy, The University of Texas at Austin, 2515 Speedway, Stop C1400, Austin, TX 78712, USA
[6] Department of Astronomy and Astrophysics, The Pennsylvania State University, University Park, PA 16802, USA
[7] Institute for Gravitation and the Cosmos, The Pennsylvania State University, University Park, PA 16802, USA
[8] Max-Planck Institut für extraterrestrische Physik, Giessenbachstrasse 1, D-85748 Garching, Germany
[9] University Observatory, Fakultät für Physik, Ludwig-Maximilians University Munich, Scheiner Strasse 1, D-81679 Munich, Germany
[10] Department of Physics and Astronomy, Rutgers, The State University of New Jersey, Piscataway, NJ 08854, USA
[11] McDonald Observatory, University of Texas at Austin, 2515 Speedway, Stop C1402, Austin, TX 78712, USA
[12] Department of Physics and Astronomy, University College London, Gower Street, London WC1E 6BT, UK
[13] Physics Department, NYC College of Technology, 300 Jay Street, Brooklyn, NY 11201, USA
[14] Center for Computational Astrophysics, Flatiron Institute, New York, NY 10010, USA
[15] Astrophysics, Department of Physics, Keble Road, Oxford, OX1 3RH, UK
[16] Department of Physics & Astronomy, University of the Western Cape, Private Bag X17, Bellville, Cape Town, 7535, South Africa
[17] Lawrence Berkeley National Laboratory, 1 Cyclotron Road, Berkeley, CA 94720, USA
Received 2021 May 24; revised 2021 August 1; accepted 2021 August 16; published 2021 November 29

Abstract

We present Lyα and ultraviolet (UV)-continuum luminosity functions (LFs) of galaxies and active galactic nuclei (AGNs) at $z = 2.0$–3.5 determined by the untargeted optical spectroscopic survey of the Hobby–Eberly Telescope Dark Energy Experiment (HETDEX). We combine deep Subaru imaging with HETDEX spectra resulting in 11.4 deg^2 of fiber spectra sky coverage, obtaining 18,320 galaxies spectroscopically identified with Lyα emission, 2126 of which host type 1 AGNs showing broad (FWHM > 1000 km s^{-1}) Lyα emission lines. We derive the Lyα (UV) LF over 2 orders of magnitude covering bright galaxies and AGNs in $\log L_{\mathrm{Ly}\alpha}/[\mathrm{erg\ s^{-1}}] = 43.3$–$45.5$ ($-27 < M_{\mathrm{UV}} < -20$) by the $1/V_{\mathrm{max}}$ estimator. Our results reveal that the bright-end hump of the Lyα LF is composed of type 1 AGNs. In conjunction with previous spectroscopic results at the faint end, we measure a slope of the best-fit Schechter function to be $\alpha_{\mathrm{Sch}} = -1.70^{+0.13}_{-0.14}$, which indicates that α_{Sch} steepens from $z = 2$–3 toward high redshift. Our UV LF agrees well with previous AGN UV LFs and extends to faint-AGN and bright-galaxy regimes. The number fraction of Lyα-emitting objects (X_{LAE}) increases from $M^*_{\mathrm{UV}} \sim -21$ to bright magnitude due to the contribution of type 1 AGNs, while previous studies claim that $X_{\mathrm{Ly}\alpha}$ decreases from faint magnitudes to M^*_{UV}, suggesting a valley in the $X_{\mathrm{Ly}\alpha}$–magnitude relation at M^*_{UV}. Comparing our UV LF of type 1 AGNs at $z = 2$–3 with those at $z = 0$, we find that the number density of faint ($M_{\mathrm{UV}} > -21$) type 1 AGNs increases from $z \sim 2$ to 0, as opposed to the evolution of bright ($M_{\mathrm{UV}} < -21$) type 1 AGNs, suggesting AGN downsizing in the rest-frame UV luminosity.

Unified Astronomy Thesaurus concepts: High-redshift galaxies (734); Galaxy evolution (594); Lyman-alpha galaxies (978); Active galactic nuclei (16)

1. Introduction

At high redshift, Lyα emitters (LAEs) are a widely studied population of objects that feature strong Lyα (Lyα λ1216 Å) emission lines (e.g., Rhoads et al. 2000; Gronwall et al. 2007; Pentericci et al. 2009; Ouchi et al. 2020). Typical LAEs are interpreted as young ($\lesssim$50 Myr), low-mass ($\lesssim 10^{10}$ $M_\odot$) galaxies with high star formation rates (SFRs) of $\sim$1–100 $M_\odot$ yr^{-1} (e.g., Nagao et al. 2005; Gawiser et al. 2006; Finkelstein et al. 2007, 2008, 2009; Ono et al. 2010a, 2010b; Kashikawa et al. 2012; Harikane et al. 2018). Such properties make LAEs important tracers for galaxy formation at the low-mass end of the spectrum in the early universe, complementary to the continuum-selected Lyman break galaxies (LBGs) that are relatively massive.

A key statistical property of LAEs is the luminosity function (LF), which is defined as the number density as a function of luminosity. The LAE LFs and their evolution can provide valuable insights into the evolution of young, star-forming (SF) galaxies over cosmic time. Over the past few decades, LAEs have been identified and studied with LFs over the redshift range $z \sim$ 0–9 using deep narrowband (e.g., Gronwall et al. 2007; Ouchi et al. 2008, 2010; Konno et al. 2016, 2018; Tilvi et al. 2020) and spectroscopic surveys (e.g., Blanc et al. 2011; Cassata et al. 2011; Zheng et al. 2013; Drake et al. 2017; Herenz et al. 2019). These studies have found that at Lyα luminosity $L_{\mathrm{Ly}\alpha} \lesssim 10^{43}$ erg s^{-1}, the Lyα LF of LAEs can be described by the Schechter function (Schechter 1976),

$$\phi_{\mathrm{Sch}}(L)\,d\log L = \ln 10\ \phi^*_{\mathrm{Sch}} \left(\frac{L}{L^*_{\mathrm{Sch}}}\right)^{\alpha_{\mathrm{Sch}}+1} \exp\left(-\frac{L}{L^*_{\mathrm{Sch}}}\right) d\log L. \quad (1)$$

The values of $L^*_{\rm Sch}$, $\alpha_{\rm Sch}$, and $\phi^*_{\rm Sch}$ represent the characteristic luminosity, faint-end slope, and characteristic number density, respectively. Comparing Lyα LFs at different epochs also shows the redshift evolution of LAEs. From $z\sim0$ to 3, the number density of LAEs increases rapidly (e.g., Deharveng et al. 2008). At $z\sim3$–6, there is little evolution in the number density of LAEs (e.g., Dawson et al. 2004; Ouchi et al. 2008). Beyond $z\sim6$, the observed number density of LAEs begins to decrease due to the resonant scattering of Lyα photons by the increasing neutral hydrogen (H I) fraction in the intergalactic medium toward the epoch of reionization (e.g., Kashikawa et al. 2006; Hu et al. 2010; Itoh et al. 2018), although there is also evidence suggesting no evolution of Lyα LF from $z=5.7$ to 6.5 (e.g., Malhotra & Rhoads 2004).

Despite the efforts of previous studies of the Lyα LFs, several open questions still remain. One is the steepness of the faint-end slope of the Lyα LFs that describes the fraction of faint galaxies relative to brighter ones. Theoretical models of hierarchical structure formation predict that low-mass galaxies are more dominant at higher redshift, which results in a steeper faint-end slope. Such a redshift evolution of the faint-end slope has been identified in the ultraviolet (UV)-continuum LF (hereafter UV LF) of LBGs (e.g., Bouwens et al. 2015; Finkelstein et al. 2015). Since the dust attenuation of Lyα emission in the interstellar medium (ISM) becomes larger toward fainter UV luminosity (e.g., Ando et al. 2006; Ouchi et al. 2008) and higher redshift (e.g., Blanc et al. 2011; Hayes et al. 2011), the observed faint-end slope of the Lyα LF is expected to be steeper than that of the UV LF toward higher redshift. However, the faint-end slope of the Lyα LF is poorly constrained in the previous studies due to the large uncertainty of contamination in photometric LAE samples and the limited spectroscopic LAE samples.

Another open question in relation to the Lyα LF is the shape of the bright end. Several studies have attempted to statistically characterize the bright LAEs with $\log L_{\rm Ly\alpha}/[{\rm erg\ s^{-1}}]\gtrsim43.5$ based on photometrically selected samples, reaching various conclusions. For example, Konno et al. (2016) identified an excess in the number density with respect to the Schechter function at the bright end of their Lyα LFs at $z=2.2$. Such an excess was also found in Lyα LFs over other redshift ranges (e.g., Wold et al. 2017; Zheng et al. 2017; Sobral et al. 2017, 2018a and Matthee et al. 2017) showed a similar but less significant bright-end excess at $z=2$–3 and demonstrated that such an excess can be fitted by a power law. At similar redshifts, Spinoso et al. (2020) found ∼14,500 LAEs with $\log L_{\rm Ly\alpha}/[{\rm erg\ s^{-1}}]>43.3$. The Ly$\alpha$ LFs of their bright LAEs are described by Schechter exponential decays with $\log L^*_{\rm Sch}/[{\rm erg\ s^{-1}}]\sim44.5$–44.8. Despite these efforts, the precise shape of the Lyα LF, especially at the bright end, is in need of further constraints from spectroscopic studies.

Along with the shape of the Lyα LF at the bright end, it is also important to understand the nature of the extreme objects that cause the bright-end excess. Although the differential attenuation of Lyα photons in the clumsy ISM may cause the Lyα LFs to have a non-Schechter shape, more evidence attributes the bright-end excess to the existence of Lyα-emitting active galactic nuclei (AGNs). The AGN activity peaks at $z\sim2$–3 (Hasinger 2008), which may result in the contribution of faint AGNs to the LAE population. Such a scenario is supported by results based on the spectroscopic follow-ups and multiwavelength detections of small samples of photometrically selected, bright LAEs. In particular, Ouchi et al. (2008) showed that their bright LAEs at $z=3.1$–3.7 with $L_{\rm Ly\alpha}=10^{43.3-43.6}\,{\rm erg\ s^{-1}}$ always host AGNs. Sobral et al. (2018b) conducted spectroscopic observations on 21 luminous LAEs at $z\sim2$–3 and concluded that the AGN fraction increases with Lyα luminosity. Similar trends are also observed through the number fraction of radio- and X-ray-detected LAEs (e.g., Matthee et al. 2017; Calhau et al. 2020). The AGNs trace the growth of black holes (BHs) at the centers of galaxies and may provide feedback that suppresses star formation in galaxies (e.g., Fabian 2012; Merloni & Heinz 2013). Hence, they are keys to understanding galaxy evolution.

In this paper, we investigate the Lyα and UV LFs of LAEs at $z\sim2$–3 detected by the Hobby–Eberly Telescope Dark Energy Experiment (HETDEX) survey (Hill et al. 2008; Gebhardt et al. 2021, in preparation; Hill et al. 2021, in preparation). Combining the untargeted, wide-field integral field spectroscopic (IFS) data of HETDEX and deep ground-based imaging data of the Subaru Hyper Suprime-Cam (HSC), we explore the low number density regime for both Lyα and UV LFs, where the LAE population consists of both SF galaxies and AGNs.

This paper is arranged as follows. Section 2 describes the details of the HETDEX survey and the spectroscopic data included in this paper. Our LAE samples are presented in Section 3. In Section 4, we derive the Lyα LF at $z=2.0$–3.5. We also show the spectroscopic properties and UV LF of type 1 AGNs in our LAE samples. We discuss the evolution of the Lyα LF of LAEs and the UV LF of type 1 AGNs in Section 5. Throughout this paper, we use AB magnitudes (Oke 1974) and the cosmological parameters of $(\Omega_{\rm m},\,\Omega_\Lambda,\,h)=(0.3,\,0.7,\,0.7)$.

2. Observations and Data

2.1. HETDEX Survey

HETDEX is an untargeted IFS survey designed to measure the expansion history of the universe at $z\sim1.9$–3.5 by mapping the 3D positions of around 1 million LAEs. The survey started in 2017 January and is scheduled to finish in 2024. On completion, it will cover ∼540 deg^2 of sky area that is divided into northern ("Spring") and equatorial ("Fall") fields. The corresponding survey volume is ∼11 comoving Gpc^3. The survey is conducted with the Visible Integral-field Replicable Unit Spectrograph (VIRUS; Hill et al. 2018a; Hill et al. 2021, in preparation), which is fed by fibers from the prime focus of the upgraded 10 m Hobby–Eberly Telescope (HET; Ramsey et al. 1994; Hill et al. 2018b; Hill et al. 2021, in preparation). VIRUS is a replicated integral field spectrograph (Hill 2014) that consists of 156 identical spectrographs (arrayed as 78 units, each with a pair of spectrographs) fed by 34,944 fibers, each 1.″5 diameter, projected on the sky. VIRUS has a fixed spectral bandpass of 3500–5500 Å and resolving power $R\sim800$ at 4500 Å (Hill et al. 2018a; Hill et al. 2021, in preparation). The fibers are grouped into 78 integral field units (IFUs; Kelz et al. 2014), each with 448 fibers in a common cable. There is one IFU covering a $51''\times51''$ area for each two-channel spectrograph unit. The fibers are illuminated directly at the f/3.65 prime focus of HET and arrayed within each IFU with a 1/3 fill factor such that an observation requires three exposures with dithers in sky position to fill in the areas of the IFUs. For HETDEX, the exposure time is 3 × 360 s for each pointing set. The IFUs are arrayed in a grid pattern with 100″ spacing within the central 18′ diameter of the field of the upgraded HET and fill this area with an ∼1/4.5 fill factor. A detailed technical description of

Table 1
Flags for the HSC *r*-band Source Catalog

Parameter	Value	Notes
r_pixelflags_edge	False	Source is outside usable exposure region
r_pixelflags_interpolatedcenter	False	Interpolated pixel in the source center
r_pixelflags_saturatedcenter	False	Saturated pixel in the source center
r_pixelflags_crcenter	False	Cosmic ray in the source center
r_pixelflags_bad	False	Bad pixel in the source footprint
r_pixelflags_bright_objectcenter	False	Source center is close to BRIGHT_OBJECT pixels
r_pixelflags_bright_object	False	Source footprint includes BRIGHT_OBJECT pixels
r_pixelflags	False	General failure flag
detect_istractinner	True	True if source is in the inner region of a coadd tract
detect_ispatchinner	True	True if source is in the inner region of a coadd patch

the HET wide-field upgrade and VIRUS and their performance is presented in Hill et al. (2021, in preparation).

The data presented in this paper were obtained as part of the internal HETDEX Data Release 2 (iHDR2; Gebhardt et al., 2021, in preparation). The iHDR2 includes 3086 exposure sets taken between 2017 January and 2020 June with between 16 and 71 active IFUs. From these data, we select 1862 exposure sets whose footprints are covered by Subaru/HSC imaging data. The total area is 57 $\deg^2$ with spatial filling factors of $\sim$20%, which yields an effective area of 11.4 $\deg^2$, corresponding to $\sim 2.0 \times 10^8$ comoving Mpc^3 for the redshift range of $2.0 < z < 3.5$.

2.2. Subaru/HSC Imaging

To provide better measurements on the UV continua of LAEs at $z = 1.9$–3.5, we utilize the *r*-band imaging data taken by Subaru/HSC. The HSC *r*-band filter covers the wavelength range of 5500–7000 Å. For sources at $z = 1.9$–3.5, the HSC *r*-band magnitudes serve as a good estimation for the UV continua, while the HETDEX spectra can detect the Lyα emission lines.

The *r*-band imaging data in this study are taken from two surveys, the HSC *r*-band imaging survey for HETDEX (hereafter the HETDEX-HSC survey) and the Subaru Strategic Program (HSC-SSP; Aihara et al. 2018). The HETDEX-HSC survey has obtained imaging data of an $\sim$250 $\deg^2$ area in the Spring field. The observations of the HETDEX-HSC survey were carried out in 2015–2018 (S15A, S17A, S18A; PI: A. Schulze) and 2019–2020 (S19B; PI: S. Mukae), with a total observing time of 3 nights and seeing sizes of 0.″6–1.″0. The 5σ limiting magnitude in a 3.″0 diameter aperture is $r = 25.1$ mag.

In addition to the HETDEX-HSC survey, we also exploit the *r*-band imaging data in the public data release 2 (PDR2) of HSC-SSP (Aihara et al. 2019). The HSC-SSP PDR2 includes deep multicolor imaging data of a sky area of $\sim$300 $\deg^2$ taken over the span of 300 nights. The *r*-band imaging data of HSC-SSP PDR2 have an average seeing size of $\sim$0.″7. The 5σ limiting magnitude for the 3.″0 diameter aperture is $r = 25.8$ and 27.7 mag in the wide (W) and ultradeep (UD) layers, respectively. The data reduction and source detection of the HETDEX-HSC and HSC-SSP surveys are conducted with `hscPipe` (Bosch et al. 2018) version 6.7.

3. Samples

In this section, we provide details of how we construct LAE samples with iHDR2. Although iHDR2 includes a curated emission line catalog (hereafter the HETDEX emission line catalog) that is based on the blind search for detections from all spectral and spatial elements (Gebhardt et al. 2021, in preparation), the HETDEX emission line catalog fails to recover some of the previously identified type 1 AGNs with broad emission lines. This is because the HETDEX emission line catalog is optimized for typical SF galaxies with narrow emission lines. Given the large HETDEX data set, current attempts to include broad emission line candidates remain challenging, as this could introduce artifacts such as continuum between two close absorption lines and humps caused by calibration issues. With the challenge of selecting broad-line LAEs from the HETDEX emission line catalog, we construct a new emission line catalog based on the iHDR2 reduced fiber spectra and the deep HSC *r*-band imaging data (hereafter the HSC-detected catalog). Our detection algorithm performs emission line detection in a variety of wavelength bins at the positions of continuum sources in the HSC *r*-band imaging data. Because the spatial positions are determined, the algorithm is able to detect broad emission line candidates while limiting the number of artifacts. In Section 3.1, we describe the HETDEX emission line and HSC-detected catalogs. We combine the HETDEX emission line and HSC-detected catalogs, making an emission line catalog with a signal-to-noise ratio $(S/N) > 5.5$ that does not miss broad emission lines. In Section 3.2, we construct the LAE sample from the combined catalog. Section 3.3 describes our spectroscopic follow-ups on LAE candidates selected in Section 3.2.

3.1. Emission Line Catalogs

3.1.1. HETDEX Emission Line Catalog

The HETDEX emission line catalog (internally v2.1.1) is constructed with an automatic detection pipeline developed by the HETDEX collaboration. Details of the pipeline are introduced in Gebhardt et al. (2021, in preparation). In general, the following three steps are involved. (i) The positions of emission line candidates are determined based on a grid search in all spatial and spectral elements of the reduced HETDEX fiber spectra with bin sizes of 0.″5 in the spatial direction and 4 Å in the wavelength direction. (ii) At the positions of detections, 1D spectra are extracted, and emission line fits are conducted to measure the central wavelengths, fluxes, and line widths of emission line candidates. (iii) Emission line candidates are further screened based on the χ^2 of the fitting results, S/N, and line widths.

From the HETDEX emission line catalog, we obtain emission line candidates with $S/N > 5.5$ and wavelengths of 3666 Å $< \lambda <$ 5490 Å. The $S/N > 5.5$ cut allow us to obtain a relatively clean emission line sample with limited false detections. We apply the wavelength cut to keep consistency with our HSC-detected sources (Section 3.1.2). We also require

Table 2
Summary of LAE Samples

Field	(R.A., decl.) (deg)	Area[a] (arcmin^2)	$N_{\rm NL\ LAE}$	$N_{\rm BL\ LAE}$	$N_{\rm C\ LAE}$	Imaging Data	$r_{5\sigma}$[b] (mag)
dex-Spring	(205.0, 51.3)	29,470	11,966	1532	13,498	HET-HSC	25.1
dex-Fall	(21.5, 0.0)	11,542	4129	584	4713	HSC-SSP(W)	25.8
COSMOS	(150.2, 2.3)	133	99	10	109	HSC-SSP(UD)	27.7
Total		41,145	16,194	2126	18,320		

Notes.
[a] Effective survey area covered by HETDEX fibers.
[b] 5σ limiting magnitude of imaging data for a $3''$ diameter aperture.

the emission line candidates to locate within the areas covered by HSC *r*-band imaging data. We measure the rest-frame UV continua of emission line candidates using the HSC *r*-band imaging data. We cross-match the emission line candidates with the HSC *r*-band detected sources within $2''$ radii and use the $3''$ diameter aperture magnitudes of the *r*-band–detected sources as the continuum flux density. If there are no *r*-band–detected counterparts, we use the 5σ limiting magnitude (Table 2) as the upper limit of the continuum flux density.

To check the possible contamination from false detections such as cosmic rays, sky residuals, and bad pixels, we randomly select 412 emission line candidates and conduct visual classification. We find that 17/412 (4%) emission line candidates are false detections. This indicates a negligible fraction of false detections in our HETDEX emission line catalog. We obtain 138,314 emission line candidates from the HETDEX emission line catalog.

3.1.2. HSC-detected Catalog

We construct our HSC-detected emission line catalog based on the *r*-band imaging data of the HETDEX-HSC and HSC-SSP surveys. From the *r*-band–detected source catalog, we select isolated or cleanly deblended sources. We then require that none of the central 3×3 pixels are saturated, and none of the central 3×3 pixels are severely affected by very bright neighboring sources. We also remove objects with flags indicating failed centroid position measurements. The selection criteria that we use for this purpose are listed in Table 1. We then limit the catalog to the 2,972,750 sources whose S/N is larger than 5 based on their $3''$ diameter aperture magnitudes.

We extract 1D source spectra $F_{\rm source}(\lambda)$ at the positions of the objects in the *r*-band source catalog from the reduced HETDEX fiber spectra. We assume that the 2D distribution of light on the focal plane for point sources is described by the Moffat point-spread function (PSF; e.g., Moffat 1969; Trujillo et al. 2001) and calculate the PSF value $_{pi}$ at the position of the fiber *i*. We sum up the fiber spectra within a radius of $2\farcs5$ around the positions of the objects in the *r*-band source catalog using the equation

$$F_{\rm source}(\lambda) = \frac{\sum_{i=1}^{n} F_i(\lambda) p_i}{\sum_{i=1}^{n} p_i^2}, \quad (2)$$

where $F_i(\lambda)$ is the spectrum of fiber *i*. Since the noise levels of the fiber spectra at the edge of the HETDEX spectral range is >3 times higher than the median level, we only use the data in the spectral range of 3666 Å $< \lambda <$ 5490 Å. This wavelength range corresponds to the Lyα redshift of $2.0 < z < 3.5$.

We perform emission line detection and flux measurement on the source spectra. We first subtract continua from the source spectra with the median filter and sigma clipping method. To include the broad emission lines, we then repeatedly scan and measure the S/N of the source spectra within various wavelength bins (6, 10, 18, 34, and 110 Å). We require the emission lines to have S/N > 5.5 in any of the wavelength bins. We fit single Gaussian profiles to measure the central wavelengths and FWHMs of the emission lines. Since the shapes of the Lyα emission lines are sometimes asymmetric or have double peaks (e.g., Dijkstra et al. 2006; Matthee et al. 2018), we additionally fit double Gaussian profiles. For flux measurements, the choice between the single and double Gaussian models is determined by visual inspections.

To remove false detections such as cosmic rays, sky residuals, and bad pixels, we first apply the machine-learning (ML) classifier (Sakai 2021, Sakai et al., in preparation) that takes the 2D spectrum of each emission line candidate as input and returns a score from zero (false detections) to 1 (real detections). We test the reliability of our ML classifier by visually classifying 14,276 randomly selected detections. Among the 14,276 detections, 1725 (12,551) are classified as real (false) detections. Comparing our visual classification with the scores given by the ML classifier, we find that a score higher than 0.1 effectively removes 5762/12,551 (46%) false detections while recovering 1624/1725 (94%) real detections. We thus require a score higher than 0.1. This initial screening process yields to 385,493 emission line candidates from the HSC-detected catalog. We conduct visual classification to remove the remaining false detections in the HSC-detected catalog after selecting LAE candidates in Section 3.2.

3.2. LAE Selection

It is challenging to distinguish Lyα from [O II] λ3727 lines with the HETDEX spectral data alone for three reasons. First, the spectral resolution of VIRUS is not high enough to distinguish between the asymmetric Lyα and the blended [O II] doublet based on the skewness of their emission line profiles (Hill et al. 2021, in preparation; Gebhardt et al. 2021, in preparation). Second, many LAEs at $2.06 \leqslant z \leqslant 3.5$ and [O II] emitters at $0.1 \leqslant z \leqslant 0.5$ appear as single-line emitters in the HETDEX spectra whose range is 3500–5500 Å. Finally, the relatively low sensitivity makes it difficult to precisely measure the continuum of sources within the spectrum alone to select LAEs with the rest-frame equivalent width (EW_0) cut technique (e.g., Gronwall et al. 2007; Ouchi et al. 2008; Konno et al. 2016) that is widely used.

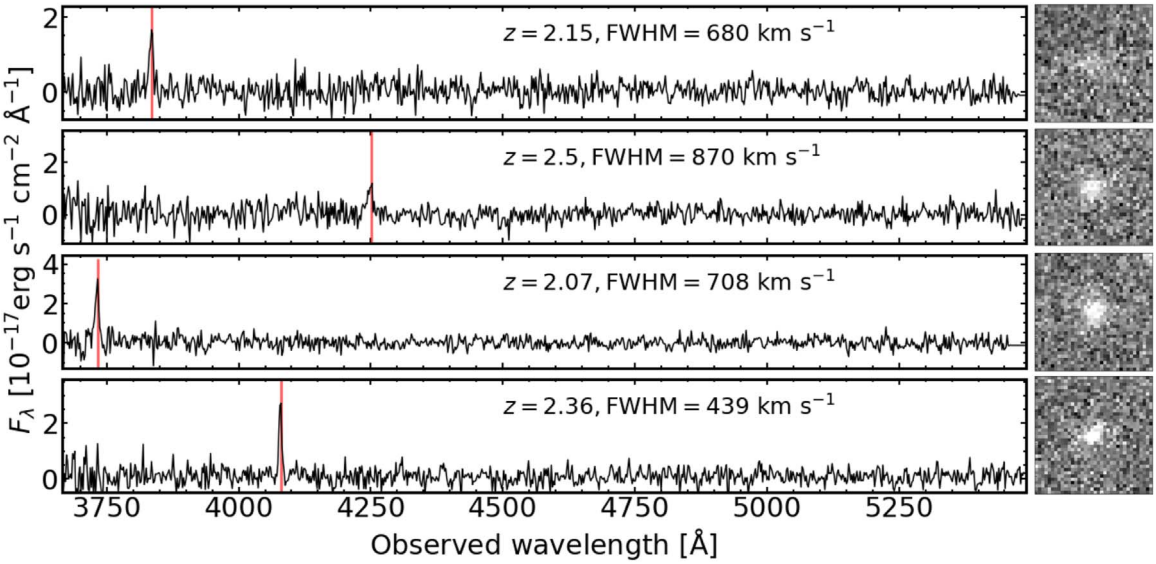

Figure 1. Examples of NL LAEs. The left panels show the HETDEX spectra (black lines) of the NL LAEs. The redshifts and FWHMs are indicated at the top of each spectrum. The red solid lines represent the wavelengths of Lyα emission lines. The right panels denote the $8'' \times 8''$ r-band images from the HETDEX-HSC survey. North is up, and east is to the left.

To resolve this problem, we identify Lyα emission lines from the final emission line catalog based on the EW_0 calculated from the flux measured from HETDEX spectra and continuum measured from HSC r-band imaging data. Our goal is to select Lyα emission lines from both SF galaxies and AGNs. We first require the EW_0 of the emission line to be greater than 20 Å, assuming Lyα redshifts. This Lyα EW_0 cut is similar to previous LAE studies (e.g., Gronwall et al. 2007; Konno et al. 2016). We estimate continuum flux densities at the wavelength of Lyα from the HSC r-band magnitudes with the assumption of a flat UV continuum (i.e., $F_\nu = \text{const}$). This is a typical UV spectrum assumed in studies of high-z galaxies including LAEs (e.g., Ouchi et al. 2008; Konno et al. 2016, 2018). At $z = 2$–3.5, the r-band central wavelength corresponds to the rest frame 1400–2000 Å. If we assume a UV slope of -0.5 to 0.5, the resulting UV flux changes by only 20%.

We notice that with this Lyα EW_0 cut, there are still a consistent number of foreground contaminants. Most of these contaminants are the [O II] (C IV λ1549, [C III] λ1909, and Mg II λ2798) emission lines from low-z SF galaxies (AGNs). Because the sources of contamination are different for SF galaxies and AGNs, it is difficult to select Lyα emission lines from SF galaxies and AGNs with one set of criteria. To resolve this problem, we use the FWHM of the emission line to separate SF galaxies and type 1 AGNs (e.g., Netzer 1990). We divide our $EW_0 > 20$ Å emission line sample into two subsamples, narrow-line (NL; FWHM $\leqslant 1000\,\mathrm{km\,s^{-1}}$) and broad-line (BL; FWHM $> 1000\,\mathrm{km\,s^{-1}}$), that mainly contain SF galaxies and type 1 AGNs, respectively. We select NL (BL) LAEs from NL (BL) subsamples, combining them to make our combined LAE (C LAE) sample. Sections 3.2.1 and 3.2.2 discuss NL- and BL LAE selection, respectively. We summarize our LAE sample in Section 3.2.3.

3.2.1. NL LAE Subsample

We select NL LAEs from the NL emission line catalog with $EW_0 > 20$ Å and FWHM $\leqslant 1000\,\mathrm{km\,s^{-1}}$. For the typical SF galaxy, the most prominent emission lines within the HETDEX spectral range of 3500–5500 Å could be Lyα, [O II], Hβ λ4863, and [O III] λ4960, λ5007. Assuming the single emission line to be Hβ at $z = 0$–0.13 ([O III] at $z = 0$–0.10), the HETDEX spectra would cover other strong emission lines, such as [O II] (Hβ) on the blue (red) side of the spectrum. Because other emission lines of LAEs at $z = 1.9$–3.5 ([O II] emitters at $z = 0.13$–0.48) lie beyond the HETDEX wavelength coverage, LAEs ([O II] emitters) would appear as single-line emitters in the HETDEX spectra. For this reason, LAEs at $z = 2.1$–3.5 and [O II] emitters at $z = 0$–0.5 are indistinguishable in the HETDEX spectra for a typical SF galaxy. To isolate LAEs from [O II] emitters, we apply the Bayesian statistical method (Leung et al. 2017), as modified and implemented by Farrow et al. (2021) and Davis et al. (in preparation). The Bayesian statistical method calculates the probability P_{LAE} ($P_{[\mathrm{O\,II}]}$) that a given source is an LAE ([O II] emitter) based on the EW_0, luminosity, and wavelength of the source. The probability ratio $P_{\mathrm{LAE}}/P_{[\mathrm{O\,II}]}$ serves as the LAE selection criterion. We test various possible LAE selection criteria ($P_{\mathrm{LAE}}/P_{[\mathrm{O\,II}]} > 1$, 2, 5, 10, 20) with the HETDEX iHDR2 data, where 37 (10) spectroscopically and photometrically identified LAEs (foreground contaminants) are included in our emission line catalog (e.g., Kriek et al. 2015; Laigle et al. 2016; Tasca et al. 2017) with $EW_0 > 20$ Å. For each possible LAE selection criterion, we make test samples of both confirmed LAEs and foreground contaminants that meet the criterion. We calculate fractions of confirmed LAEs (foreground contaminants) in the test samples to the total confirmed LAEs (test samples) that correspond to a sample completeness (contamination rate). We apply the criterion of $P_{\mathrm{LAE}}/P_{[\mathrm{O\,II}]} > 1$ that provides a reasonably high completeness of 76% (=28/37) and a reasonably low contamination rate of 13% (=4/32). The number of objects in our NL LAE subsample is 16,194. Figure 1 shows four examples of our NL LAEs.

3.2.2. BL LAE Subsample

We examine our BL LAE selection criteria of $EW_0 > 20$ Å and FWHM $> 1000\,\mathrm{km\,s^{-1}}$. For type 1 AGNs, the major strong permitted and semiforbidden emission lines within the

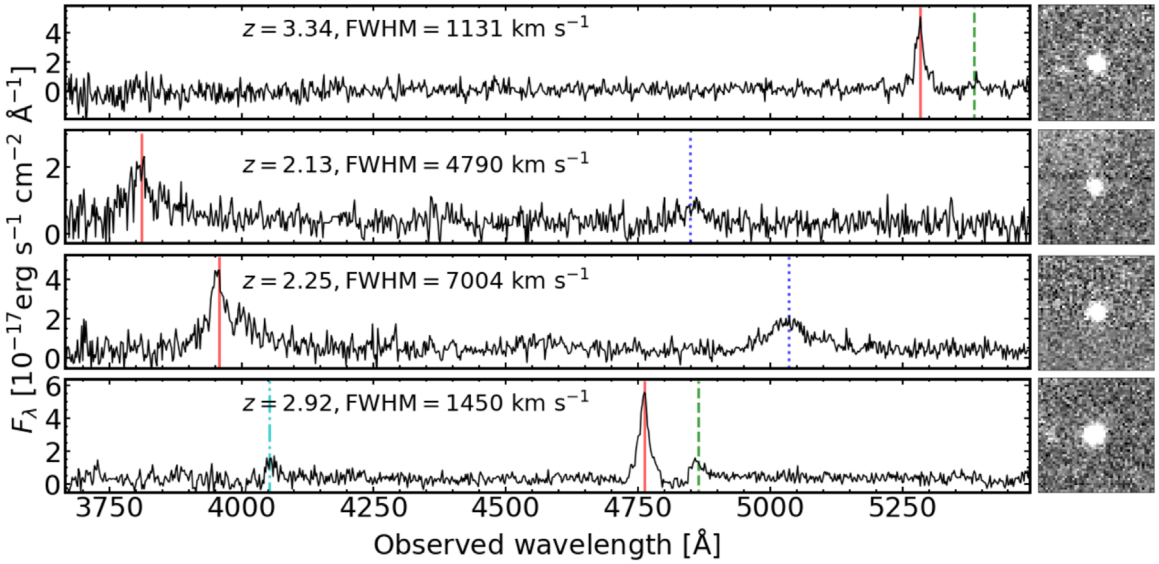

Figure 2. Same as Figure 1 but for our BL LAEs. Additionally, the blue dotted lines, green dashed lines, and cyan dashed–dotted lines represent the wavelengths of detected C IV, N V λ1240 Å, and O VI λ1035 Å emission lines, respectively.

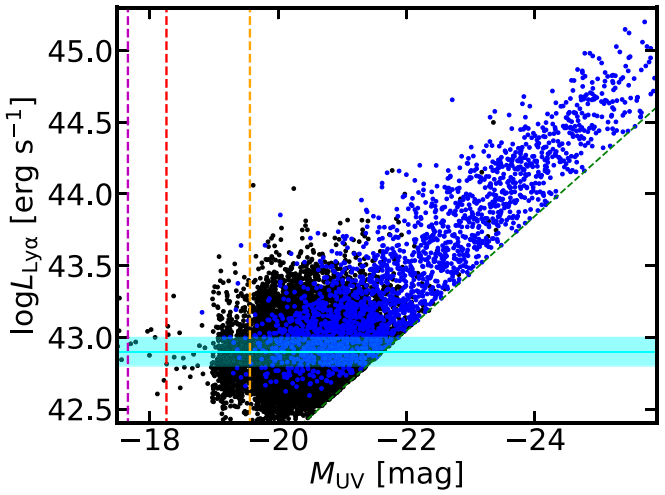

Figure 3. The $M_{\rm UV}-\log L_{{\rm Ly}\alpha}$ distributions of our LAE sample. The blue (black) data points denote BL (NL) LAEs. The green dashed line indicates our $\rm EW_0 > 20$ Å cut. The horizontal cyan line corresponds to our 50% $L_{{\rm Ly}\alpha}$ detection limit averaged over our redshift range, with the cyan shaded region indicating the 1σ uncertainty (68.27% equal-tailed credible interval). The magenta, red, and orange vertical dashed lines show the $M_{\rm UV}$ detection limits in the COSMOS, Fall, and Spring fields, respectively.

HETDEX spectral range are Lyα, C IV, [C III], and Mg II. When a single broad emission line is presented in the HETDEX spectrum, it could be Lyα from AGNs at $z = 2.0$–3.5, C IV from AGNs at $z = 1.3$–2.0, [C III] from AGNs at $z = 0.8$–1.3, or Mg II from AGNs at $z = 0.3$–1.0. However, our Lyα $\rm EW_0 > 20$ cut would require AGNs emitting C IV, [C III], and Mg II to have relatively large rest-frame EWs ($\gtrsim$25, 31, and 46 Å). Based on stacking analyses of 53 AGN spectra taken with the Wide Field Camera 3 on the Hubble Space Telescope (HST), Lusso et al. (2015) found that the typical rest-frame EWs of C IV and [C III] are about five times smaller than those of Lyα. The EWs of Mg II are also $\gtrsim$ three times smaller than those of Lyα for AGNs (Netzer 1990). Thus, the effect of contamination from low-z type 1 AGNs would be small. Discussion of the contamination of our BL LAE subsample is presented in Section 4.1. We confirm that >90% of Lyα-emitting AGNs at $2.0 < z < 3.5$ in the SDSS DR14 sample (Pâris et al. 2018) satisfy our selection criteria. We obtain the final sample of BL LAEs that contains 2126 objects. We notice that 458/2126 BL LAEs have secured redshift at $z = 2.0$–3.5 based on multiple emission lines identified in HETDEX spectra. Figure 2 shows four examples of our BL LAEs.

3.2.3. Summary of Our LAE Sample

Overall, our LAE selection criteria can be summarized as

$$\begin{aligned} &{\rm EW_0} > 20\mathring{\rm A} \text{ and} \\ &[({\rm FWHM} \leqslant 1000 \text{ km s}^{-1} \text{ and } P_{\rm LAE}/P_{[{\rm O\,II}]} > 1) \\ &\text{or } ({\rm FWHM} > 1000 \text{ km s}^{-1})]. \end{aligned} \quad (3)$$

With this set of criteria, we select 18,320 LAEs from an effective survey area of 11.4 deg^2. Our LAE sample includes 16,194 (2126) NL (BL) LAEs (Table 2). In Figure 3, we show the $M_{\rm UV}-\log L_{{\rm Ly}\alpha}$ distribution of our LAE sample.

It should be noted that our LAEs defined by Equation 3 represent an $\rm EW_0$-limited sample of both Lyα-emitting SF galaxies and AGNs at the bright $L_{{\rm Ly}\alpha}$ regime ($L_{{\rm Ly}\alpha} \gtrsim 10^{43}$ erg s^{-1}) that is different from the one of the forthcoming HETDEX studies, which produces a number count offset up to a factor of 2.

3.3. Spectroscopic Follow-up of BL LAE Candidates

To identify the potential C IV emission line of our type 1 AGN candidates, we carried out spectroscopic follow-up observations with the DEpt Imaging Multi Object Spectrograph (DEIMOS) on the Keck II Telescope (PI: Y. Harikane). With the criteria mentioned in Section 3.2.2, we select five BL LAE candidates that are visible during the observations. Our targets are summarized in Table 3.

The observations were conducted on 2020 February 25 (UT) during the filler time of Harikane et al.'s observations when their main targets were not visible. The seeing size is 0.″4–0.″8 FWHM. We used two DEIMOS masks, KAKm1 and MUKm1, to cover the five objects (Table 3) with the BAL12 filter and the 600ZD grating that is a blue spectroscopy setting for DEIMOS.

Table 3
Targets of Our DEIMOS Observations

Object ID	R.A. (J2000)	Decl. (J2000)	$z_{\mathrm{Ly}\alpha}$	$F_{\mathrm{Ly}\alpha}$ (10^{-17} erg s^{-1} cm^{-2})	r (mag)	i (mag)	Note
ID-1	14:20:11.8258	+52:51:50.4864	2.33	23.04	26.4	26.5	No emission line detected
ID-2	14:19:23.4252	+52:51:50.4864	2.08	344.3	23.5	23.4	No data available
ID-3	14:18:46.2857	+52:41:48.9012	2.27	92.55	23.3	23.2	Foreground galaxy at $z = 0.48$
ID-4	14:19:28.9898	+52:49:59.3724	2.31	67.95	22.5	22.5	Type 1 AGN
ID-5	14:18:33.0739	+52:43:13.71	2.14	42.47	23.5	23.1	Type 1 AGN

The slit width was 1.″0. The spatial pixel scale was 0.″1181 pixel^{-1}. The spectral range is 4500–8000 Å with a resolution of $R \sim 1500$. We took five (four) frames for KAKm1 (MUKm1) with a single exposure time of 2000 s. However, one frame for KAKm1 was affected by the high background sky level. We do not use this frame for our analysis. The total number of frames used for our analyses is four for each mask, KAKm1 or MUKm1. The effective exposure time is 8000 s. We acquired data of arc lamps and standard star G191B2B.

We obtained the spectroscopic data listed in Table 3. Because one out of five objects, ID-2, unfortunately falls on the broken CCD of DEIMOS, DEIMOS spectra are available for four out of five objects. Usually, the DEIMOS spectroscopic data are reduced with the `spec2d` IDL pipeline (Davis et al. 2003), which performs the bias subtraction, flat-fielding, image stacking, and wavelength calibration. However, the `spec2d` pipeline does not work in our blue spectroscopy setting due to the lack of wavelength data in the blue wavelength. We thus carry out the data reduction manually with the `IRAF` software package (Tody 1986) using the arc lamps for the wavelength calibration and standard star G91B2B for the flux calibration. We obtain 1D spectra of objects by summing up 15 pixels (∼1.″77) in the spatial direction.

We search for emission lines in both 2D and 1D spectra of the objects listed in Section 3 at the expected wavelengths using the redshifts derived from the HETDEX Lyα emission lines. We identify C IV and [C III] emission lines in two out of the four faint BL LAE candidates, ID-4 and ID-5. One of the four faint BL LAE candidates, ID-3, is a foreground galaxy at $z = 0.48$ with Hβ and [O III] emission lines identified in the DEIMOS spectrum. Another BL LAE candidate, ID-1, has no detectable emission lines in the DEIMOS spectrum. The 3σ limiting flux of C IV ([C III]) of ID-1 is 2.16 (1.87) $\times 10^{-18}$ erg s^{-1} cm^{-2}. Detailed spectroscopic properties of ID-4 and ID-5 are presented in Section 5.

4. Deriving the LFs

4.1. Contamination

We estimate the contamination rate of our NL (f_{NL}) and BL LAEs (f_{BL}) by cross-matching our sample with spectroscopic and/or photometric catalogs. We also explore the morphology of BL LAEs in archival HST imaging data. Because the number of objects available for f_{NL} (f_{BL}) estimation is not sufficient to build a redshift and luminosity correlation, we apply a uniform f_{NL} (f_{BL}) for our NL (BL) LAEs. The errors of f_{NL} and f_{BL} are based on Poisson statistics.

We estimate f_{NL} as described in Section 3.2.1. We make a subsample of 32 NL LAEs in the COSMOS field that are spectroscopically and/or photometrically identified by previous studies. We find that four out of these 32 known galaxies

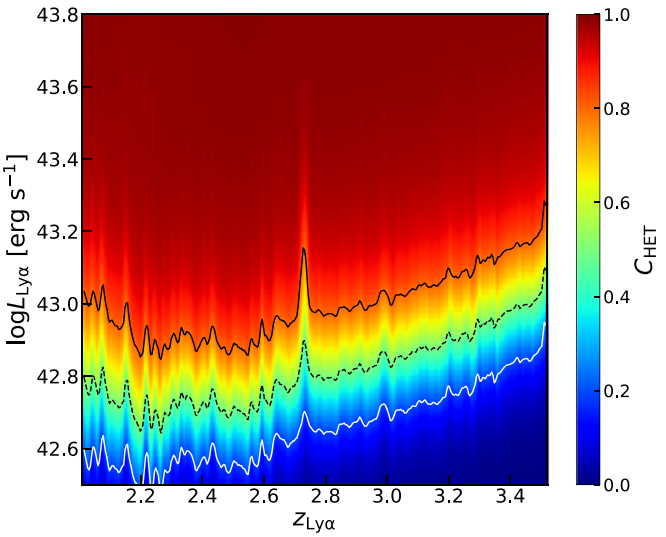

Figure 4. Completeness map of our HETDEX LAEs. The solid white line, dashed black line, and solid black line indicate the 20%, 50%, and 80% completeness levels, respectively.

are foreground contaminants. We adopt $f_{\mathrm{NL}} = 13\% \pm 8\%$ (4/32) for our NL LAE subsample.

For BL LAEs, there are two types of contamination. The first is the foreground type 1 AGN whose emission lines are redshifted to the HETDEX spectral range (Section 3.2.2). We estimate the fraction of such contamination $f_{\mathrm{BL,foreground}}$ by cross-matching our BL LAE subsample with the SDSS DR14 QSO catalog (Pâris et al. 2018). Our cross-matching results show that 111 of our BL LAEs are previously identified AGNs. Of these 111 objects, 99 are Lyα-emitting AGNs at $z = 2$–3.5. The remaining 12 objects turn out to be foreground AGNs (10 C IV–emitting AGNs at $z \sim 1.4$, one [C III]–emitting AGN at $z \sim 1.0$, and one Mg II–emitting AGN at $z \sim 0.8$). We thus apply $f_{\mathrm{BL,foreground}} = 11\% \pm 3\%$ (12/111).

The second type of contamination is the broad emission line mimicked by blended NLs emitted from close-galaxy pairs on the sky at similar wavelengths. We examine the morphology of BL LAE candidates in the COSMOS field with archival high-resolution optical images taken with the Advanced Camera for Surveys (ACS) on HST (Koekemoer et al. 2007; Massey et al. 2010). We find that three out of 10 BL LAE candidates have multiple components in the HST/ACS images that indicate possible close-galaxy pairs. Because the multiple components do not necessarily all have emission lines, we add errors allowing f_{close} to range from zero to 30% + 20% (3/10). The f_{BL} is obtained by

$$f_{\mathrm{BL}} = f_{\mathrm{foreground}} + f_{\mathrm{close}}. \quad (4)$$

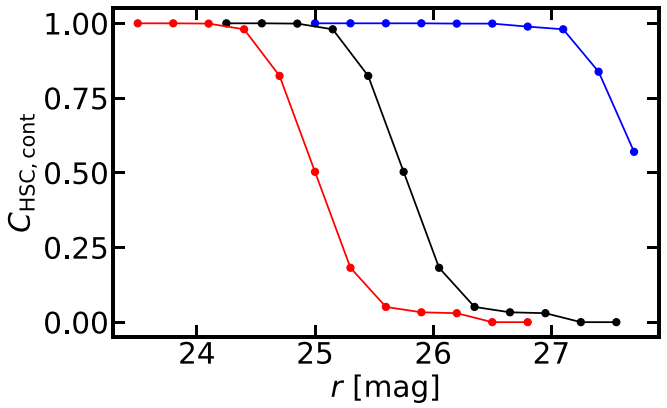

Figure 5. Completeness of our HSC r-band imaging data. The blue, black, and red lines denote the completeness of imaging data in the COSMOS, Fall, and Spring fields, respectively.

4.2. Detection Completeness

For LAEs selected from the HETDEX emission line catalog, the detection completeness ($C_{\rm HET}$) as a function of observed wavelength (λ) and emission line flux (F) is estimated from simulated LAEs inserted into real HETDEX data (Farrow et al., in preparation; Gebhardt et al., 2021, in preparation). From λ and F, we calculate Lyα redshift z and luminosity $L_{\rm Ly\alpha}$, transforming $C_{\rm HET}(\lambda, F)$ to $C_{\rm HET}(z, L_{\rm Ly\alpha})$. Figure 4 presents an example of $C_{\rm HET}(z, L_{\rm Ly\alpha})$.

For HSC-detected LAEs, the detection completeness $C_{\rm HSC}$ consists of two completeness values of the HSC r-band source detection $C_{\rm HSC,cont}$ and the HETDEX emission line detection $C_{\rm HSC,line}$, where

$$C_{\rm HSC}(z, M_{\rm UV}, L_{\rm Ly\alpha}) = C_{\rm HSC,cont}(z, M_{\rm UV}) \times C_{\rm HSC,line}(z, L_{\rm Ly\alpha}). \quad (5)$$

We derive $C_{\rm HSC,cont}$ from Kakuma (2020), who calculated the completeness of their HSC-SSP r-band imaging data as a function of magnitude. We scale their completeness function by the difference of the 5σ limiting magnitudes between their HSC-SSP wide-field data ($r_{5\sigma} = 25.8$) and our HETDEX-HSC data ($r_{5\sigma} = 25.1$), estimating the completeness function of $C_{\rm HSC_{cont}}$ that is shown in Figure 5.

We estimate $C_{\rm HSC,line}$ with Monte Carlo simulations. Specifically, we make 500 mock spectra with Gaussian line models. For each object in our sample, we fix the FWHM of the line models to the emission line fitting result given in Section 3.1.2. We then produce composite fiber spectra, assuming the 2D light distribution is described by the Moffat PSF with a $2''$ FWHM value. We add noise to the composite fiber spectra, randomly generating the noise following a Gaussian distribution function whose sigma is the median value of the noise in the fiber spectra. We perform the emission line detection on the mock spectra in the same manner as in Section 3.1.2 and calculate a $C_{\rm HSC,line}$ that is defined by the fraction of the detected artificial lines to the total mock spectra. We repeat this process with various z and $L_{\rm Ly\alpha}$, obtaining $C_{\rm HSC,line}(z, L_{\rm Lya})$. An example of $C_{\rm HSC,line}$ is shown in Figure 6.

4.3. Lyα LF

We derive the Lyα LF with our LAE sample. We apply the nonparametric $1/V_{\rm max}$ estimator (Schmidt 1968; Felten 1976) that accounts for the redshift- and luminosity-dependent selection function of our LAE sample. For the ith object in our LAE sample, $V_{{\rm max},i}$ corresponds to the maximum comoving volume inside which it is detectable. The $V_{{\rm max},i}$ value depends on the detection completeness functions $C_{\rm HET}(z, L_{\rm Ly\alpha})$ and $C_{\rm HSC}(z, M_{\rm UV}, L_{\rm Ly\alpha})$,

$$V_{{\rm max},i} = \omega \int_{z_{\rm min}}^{z_{\rm max}} C_i \frac{dV}{dz} dz, \quad (6)$$

where ω and $\frac{dV}{dz}$ denote the angular area of the survey and the differential comoving volume element, respectively. Here $z_{\rm min}$ ($z_{\rm max}$) is the lower (upper) limit of the redshift range of the survey. We calculate the $V_{\rm max}$ of each NL (BL) LAE, $V_{\rm max}^{\rm NL}$ ($V_{\rm max}^{\rm BL}$), and obtain the number densities of NL and BL LAEs in each luminosity bin with

$$\phi_{\rm NL}(\log L_{\rm Ly\alpha}) = \frac{1 - f_{\rm NL}}{\Delta(\log L_{\rm Ly\alpha})} \sum_k \frac{1}{V_{{\rm max},k}^{\rm NL}}, \quad (7)$$

$$\phi_{\rm BL}(\log L_{\rm Ly\alpha}) = \frac{1 - f_{\rm BL}}{\Delta(\log L_{\rm Ly\alpha})} \sum_k \frac{1}{V_{{\rm max},k}^{\rm BL}}, \quad (8)$$

where $\Delta(\log L_{\rm Ly\alpha})$ is the luminosity bin width and k is the number of objects in each luminosity bin. The summations in Equations (7) and (8) are performed over the k objects in each luminosity bin.

Figure 7 shows the binned Lyα LF of our LAE sample at $43.0 < \log L_{\rm Ly\alpha}[{\rm erg\ s^{-1}}] < 45.5$, where our LF reaches 50% completeness. Note that at $\log L_{\rm Ly\alpha} < 43.3\ {\rm erg\ s^{-1}}$, our Ly$\alpha$ LFs may suffer from a nonnegligible Eddington bias (Eddington 1913) that is generated from uncertainties in HETDEX spectrophotometry (Gebhardt et al. 2021, in preparation). We hence do not include the Lyα LF data points at $43.0 < \log L_{\rm Ly\alpha}/[{\rm erg\ s^{-1}}] < 43.3$ in our analysis. The error bars of our results are estimated from the quadrature sum of the Poissonian errors, errors in contamination correction, and flux measurement errors.[18] Our LFs span a wide

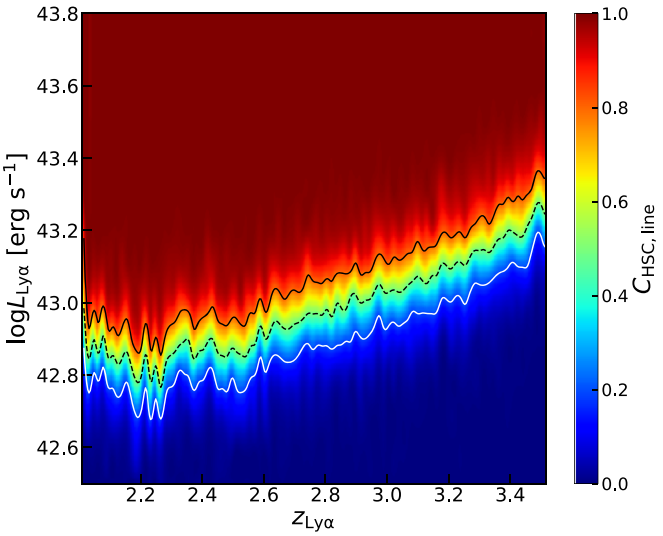

Figure 6. Same as Figure 4 but for our our HSC-detected LAEs.

[18] We also evaluate the errors in the luminosity distance measurements by considering the Lyα velocity offsets ($\Delta v_{\rm Ly\alpha}$). Typical Lyα-emitting galaxies have $\Delta v_{\rm Ly\alpha} \sim 200$–$300\ {\rm km\ s^{-1}}$ (e.g., Verhamme et al. 2018). For AGNs at $z \sim 2$–3, we investigate $\Delta v_{\rm Ly\alpha}$ based on the SDSS DR14 QSO catalog (Rakshit et al. 2020). We find the 16th, 50th, and 84th percentiles of the $\Delta v_{\rm Ly\alpha}$ distribution to be -301, 75, and $598\ {\rm km\ s^{-1}}$, respectively. Assuming $\Delta v_{\rm Ly\alpha} = 598\ {\rm km\ s^{-1}}$ would result in an uncertainty of <1% in the luminosity, which is negligible compared with the bin widths of our LFs. We hence do not consider the errors in luminosity distances.

Table 4
Fitting Results of Our Lyα LF

Model	Faint Component			Bright Component			
	α	$\log L^*$ (erg s^{-1})	$\log \phi^*$ (Mpc^{-3})	α	β	$\log L^*$ (erg s^{-1})	$\log \phi^*$ (Mpc^{-3})
Model 1 (Schechter+DPL)	$-1.70^{+0.13}_{-0.14}$	$42.87^{+0.09}_{-0.07}$	$-3.41^{+0.20}_{-0.24}$	$\mathbf{-1.23^{+0.42}_{-0.24}}$	$\mathbf{-3.06^{+0.57}_{-0.90}}$	$\mathbf{44.68^{+0.26}_{-0.40}}$	$\mathbf{-5.92^{+0.26}_{-0.32}}$
Model 2 (Schechter+Schechter)	$\mathbf{-1.69^{+0.13}_{-0.14}}$	$\mathbf{42.86^{+0.09}_{-0.07}}$	$\mathbf{-3.39^{+0.19}_{-0.23}}$	$\mathbf{-1.27^{+0.23}_{-0.19}}$	—	$\mathbf{44.85^{+0.19}_{-0.19}}$	$\mathbf{-5.96^{+0.24}_{-0.27}}$

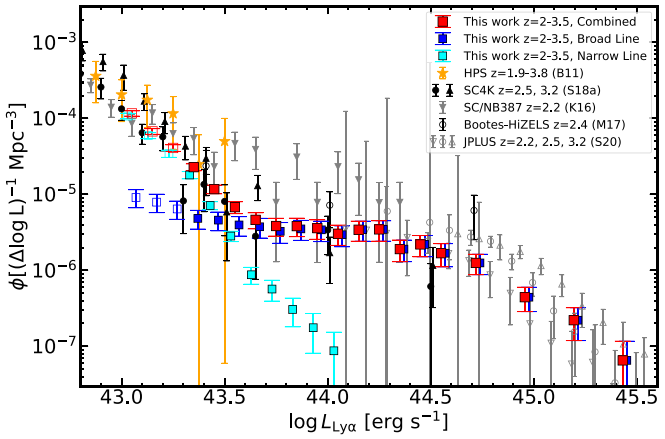

Figure 7. The Lyα LF of our NL (cyan squares), BL (blue squares) and C (red squares) LAEs within the 11.4 deg^2 survey area. Data points that may be affected by incompleteness due to Eddington bias are marked with open squares (see text). For clarity, we slightly shift the data points of the NL and BL LAEs along the abscissa. The orange stars indicate the results from the previous spectroscopic study of Blanc et al. (2011) at $1.9 < z < 3.8$ (B11). We also show the Lyα LFs at $\log L_{\rm Ly\alpha}$[erg s^{-1}] $\gtrsim$ 43.3 derived by previous photometric surveys/studies at three redshift slices of $z = 2.2$ (downward triangles), 2.4–2.5 (circles), and 3.2 (upward triangles) that are taken from Konno et al. (2016; K16, gray filled symbols), Matthee et al. (2017; M17, black open symbols), Sobral et al. (2018a; S18a, black filled symbols), and Spinoso et al. (2020; S20, gray open symbols).

Lyα luminosity range of $43.3 < \log L_{\rm Ly\alpha}/[\rm erg\ s^{-1}] < 45.5$, showing a significant bright-end excess at $\log L_{\rm Ly\alpha}/[\rm erg\ s^{-1}] \gtrsim 43.5$ that is dominated by BL LAEs that are type 1 AGNs with FWHM(Lyα) > 1000 km s^{-1}.

We compare our results in Figure 7 with those from previous studies at similar redshift and $L_{\rm Ly\alpha}$ ranges. At $z \sim 2$–3, Blanc et al. (2011) is the only work that presents the spectroscopically derived Lyα LF at $\log L_{\rm Ly\alpha}/[\rm erg\ s^{-1}] \gtrsim 43$. Due to the limited survey area of 169 arcmin^2 and the small sample of 80 LAEs, their LF does not show a bright-end hump and has large errors in the two brightest $L_{\rm Ly\alpha}$ bins at $\log L_{\rm Ly\alpha}/[\rm erg\ s^{-1}] \sim 43.3 - 43.6$. Over this $L_{\rm Ly\alpha}$ range, our results are consistent with theirs while having significantly smaller errors. At $\log L_{\rm Ly\alpha}/[\rm erg\ s^{-1}] \sim 43.3$–44, our Ly$\alpha$ LFs are comparable with previous photometric studies (e.g., Konno et al. 2016; Matthee et al. 2017; Sobral et al. 2018a) given the relatively large scatter in their results, which can possibly be attributed to the different small redshift intervals probed by these NB surveys. At the brightest end with $\log L_{\rm Ly\alpha}/[\rm erg\ s^{-1}] \gtrsim 44$, where BL LAEs dominate, our LF aligns well with Spinoso et al. (2020), supporting their suggestion that the bright LAEs in their sample are QSOs.

We conduct model fitting with our Lyα LF in Figure 7. In general, Lyα LFs at $\log L_{\rm Ly\alpha} \lesssim 43.5$ erg s^{-1} are well described by the Schechter function. Because our Lyα LF does not cover $\log L_{\rm Ly\alpha}$[erg s^{-1}] < 43.3, we constrain the faint end of the Lyα LF by including the binned Lyα LF at $z = 2$–3.2 from Cassata et al. (2011) in our fitting. The Lyα LF of Cassata et al. (2011) is derived with spectroscopically identified LAEs whose $L_{\rm Ly\alpha}$ range from 10^{41} to 10^{43} erg s^{-1}, hence complementary to our sample.

To parameterize the shape of the bright-end hump in our Lyα LF, we considering the following two models separately. In model 1, we assume the bright end follows a double power law (DPL) that is broadly used to describe the QSO/AGN UV LF (e.g., Boyle et al. 1988; Pei 1995; Boyle et al. 2000; Richards et al. 2006a; Stevans et al. 2018). The DPL is defined as

$$\phi_{\rm DPL}(L_{\rm Ly\alpha})\, d\log L_{\rm Ly\alpha} = \ln 10\ \phi^*_{\rm DPL} \left(\frac{L_{\rm Ly\alpha}}{L^*_{\rm DPL}}\right)\left[\left(\frac{L_{\rm Ly\alpha}}{L^*_{\rm DPL}}\right)^{-\alpha_{\rm DPL}} + \left(\frac{L_{\rm Ly\alpha}}{L^*_{\rm DPL}}\right)^{-\beta_{\rm DPL}}\right]^{-1} d\log L_{\rm Ly\alpha}, \quad (9)$$

where $L^*_{\rm DPL}$, $\phi^*_{\rm DPL}$, $\alpha_{\rm DPL}$, and $\beta_{\rm DPL}$ are characteristic luminosity, normalization factor, faint-end slope, and bright-end slope, respectively. In model 2, we assume the bright end can be described by a Schechter function, as suggested by Spinoso et al. (2020).

We fit our binned Lyα LF with the function of

$$\phi(L_{\rm Ly\alpha}) = \phi_{\rm faint}(L_{\rm Ly\alpha}) + \phi_{\rm bright}(L_{\rm Ly\alpha}), \quad (10)$$

where $\phi_{\rm faint}$ represents the Schechter function for the faint component, and $\phi_{\rm bright}$ is the DPL (Schechter) function of model 1 (2) for the bright component. We obtain posterior probability distributions for the free parameters in Equation (10) using the Markov Chain Monte Carlo (MCMC) technique. For the prior of $L^*_{\rm DPL}$ and $L^*_{\rm Sch}$ in $\phi_{\rm bright}$, we assume uniform distributions that are larger than $L^*_{\rm Sch}$ in $\phi_{\rm faint}$ and smaller than the maximum observed $L_{\rm Ly\alpha}$ ($10^{45.5}$ erg s^{-1}) in our Lyα LF. Since the number of our BL LAEs at the luminosity brighter than the break of the DPL in model 1 is not large, we adopt a uniform prior for $\beta_{\rm DPL}$ in model 1 covering a relatively narrow range of [−5, −2] (e.g., Kulkarni et al. 2019). We assume broad, uniform priors for the other parameters. We use the `emcee` code (Foreman-Mackey et al. 2013) for MCMC. For each parameter, we adopt the posterior median as our best-fit value and the 68.27% equal-tailed credible interval as the uncertainty. The fitting results of our two models and the best-fit functions are presented in Table 4 and Figure 8, respectively. The posterior probability distributions of the parameters of model 1 (2) are shown in Figure 9 (10). We find that model 1 can better describe the decay in our Lyα LF at $\log L_{\rm Ly\alpha}$[erg s^{-1}] $\gtrsim$ 44.8 with smaller residuals, although the differences are smaller than 1σ. To compare the performance of the two models, we also calculate the difference in the Bayesian

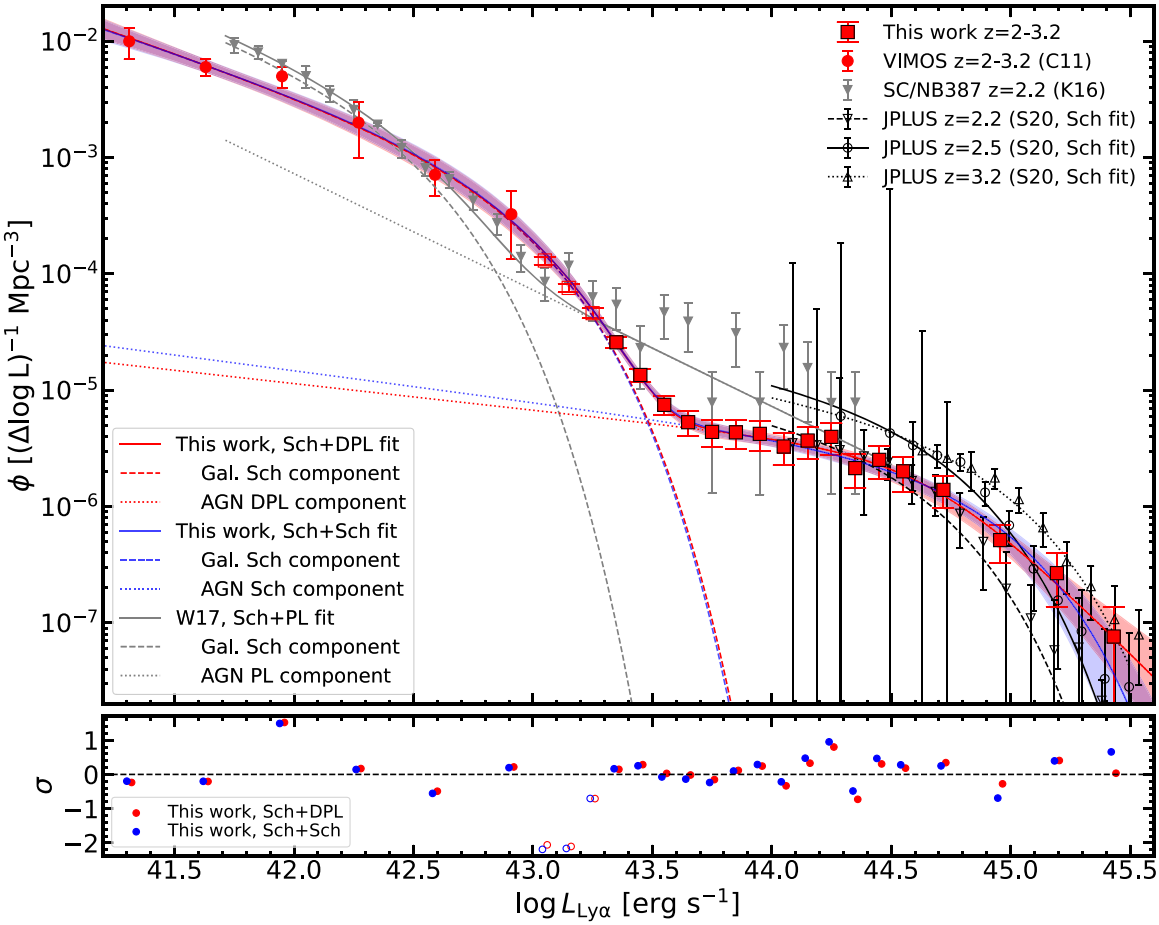

Figure 8. Top: best-fit Lyα LF of our LAE sample with $2 < z < 3.2$ (red squares) and Cassata et al. (2011) at $2.0 < z < 3.2$ (red circles). The red (blue) line shows our best-fit result of model 1 (2) with the measurements of our study and Cassata et al. (2011), with the shaded region corresponding to the 1σ uncertainty (68.27% equal-tailed credible interval). The black open downward triangles (dashed line), circles (solid line), and upward triangles (dotted line) represent the binned Lyα LFs (best Schechter fit) from Spinoso et al. (2020) at $z \sim 2.25$, 2.54, and 3.24, respectively. The gray triangles indicate the results from Konno et al. (2016). We also show with gray lines the fitting results from Wold et al. (2017) on the observed Lyα LF of Konno et al. (2016). The dashed, dotted, and solid gray lines indicate their best-fit Schechter component, power-law component, and overall LF, respectively. Bottom: residuals of models 1 (red) and 2 (blue) fit in units of the uncertainty in each luminosity bin.

information criterion (Schwarz 1978), which is defined as

$$\Delta\mathrm{BIC} = \chi_2^2 - \chi_1^2 + (k_2 - k_1)\ln N. \quad (11)$$

In Equation (11), $\chi_1^2(\chi_2^2)$ and $k_1(k_2)$ is the χ^2 and the number of free parameters of model 1(2), respectively, and N represents the number of data points that are used in the fitting. We find a ΔBIC value of -2.17, suggesting that model 1 is slightly favored over model 2. We hence choose model 1 (Schechter + DPL fit) as the best-fit model of our Lyα LF in the following discussions, although we cannot rule out a Schechter exponential decay of the Lyα LF at $\log L_{\mathrm{Ly}\alpha}[\mathrm{erg\ s^{-1}}] \gtrsim 45.8$ as described by model 2.

We compare our best-fit model of Lyα LFs with previous studies. For the bright DPL component, our faint-end slope α_{DPL} is consistent with the results from Spinoso et al. (2020), who found a weighted-average α value of -1.35 ± 0.84 over their four redshift slices. For the faint component, our results have reasonably well-constrained Schechter parameters L^*_{Sch}, α_{Sch}, and ϕ^*_{Sch} that are consistent with Cassata et al. (2011). We note that Cassata et al. (2011) fit their LF with a fixed L^* due to the lack of data at the bright end ($L_{\mathrm{Ly}\alpha} > 10^{43}\ \mathrm{erg\ s^{-1}}$). Our results provide strong constraints at $L_{\mathrm{Ly}\alpha} > L^*_{\mathrm{Sch}}$, determining the best-fit Schechter function by fitting three Schechter parameters simultaneously.

From our binned and best-fit Lyα LFs, we investigate the type 1 AGN number fraction ($f_{\mathrm{AGN,Ly}\alpha}$) of our LAE sample. Note that our $f_{\mathrm{AGN,Ly}\alpha}$ only accounts for type 1 AGNs and hence represents the lower limit. First, we calculate $f_{\mathrm{AGN,Ly}\alpha}$ with

$$f_{\mathrm{AGN,Ly}\alpha}(\log L_{\mathrm{Ly}\alpha}) = \frac{\phi_{\mathrm{BL}}(\log L_{\mathrm{Ly}\alpha})}{\phi_{\mathrm{BL}}(\log L_{\mathrm{Ly}\alpha}) + \phi_{\mathrm{NL}}(\log L_{\mathrm{Ly}\alpha})}, \quad (12)$$

where ϕ_{NL} and ϕ_{BL} are the binned LFs defined in Equations (7) and (8), respectively. We present our results with those estimated with various types of AGNs in Figure 11. Our $f_{\mathrm{AGN,Ly}\alpha}$ increases rapidly with $L_{\mathrm{Ly}\alpha}$, rising from $\sim$20% to $\sim$90%–100% from $\log L_{\mathrm{Ly}\alpha}/[\mathrm{erg\ s^{-1}}] \sim 43.3$ to $\sim$43.8. Such a trend is in good agreement with the results derived with radio- and X-ray-detected AGNs (Calhau et al. 2020). Matthee et al. (2017) also found a similar increase in $f_{\mathrm{AGN,Ly}\alpha}$ ($L_{\mathrm{Ly}\alpha}$) using X-ray-detected LAEs. At $\log L_{\mathrm{Ly}\alpha}/[\mathrm{erg\ s^{-1}}] \sim 43.6$–44.4, their results are lower than ours, which may be attributed to their relatively shallow X-ray and Lyα data (Calhau et al. 2020). Another study that discusses such an increase in

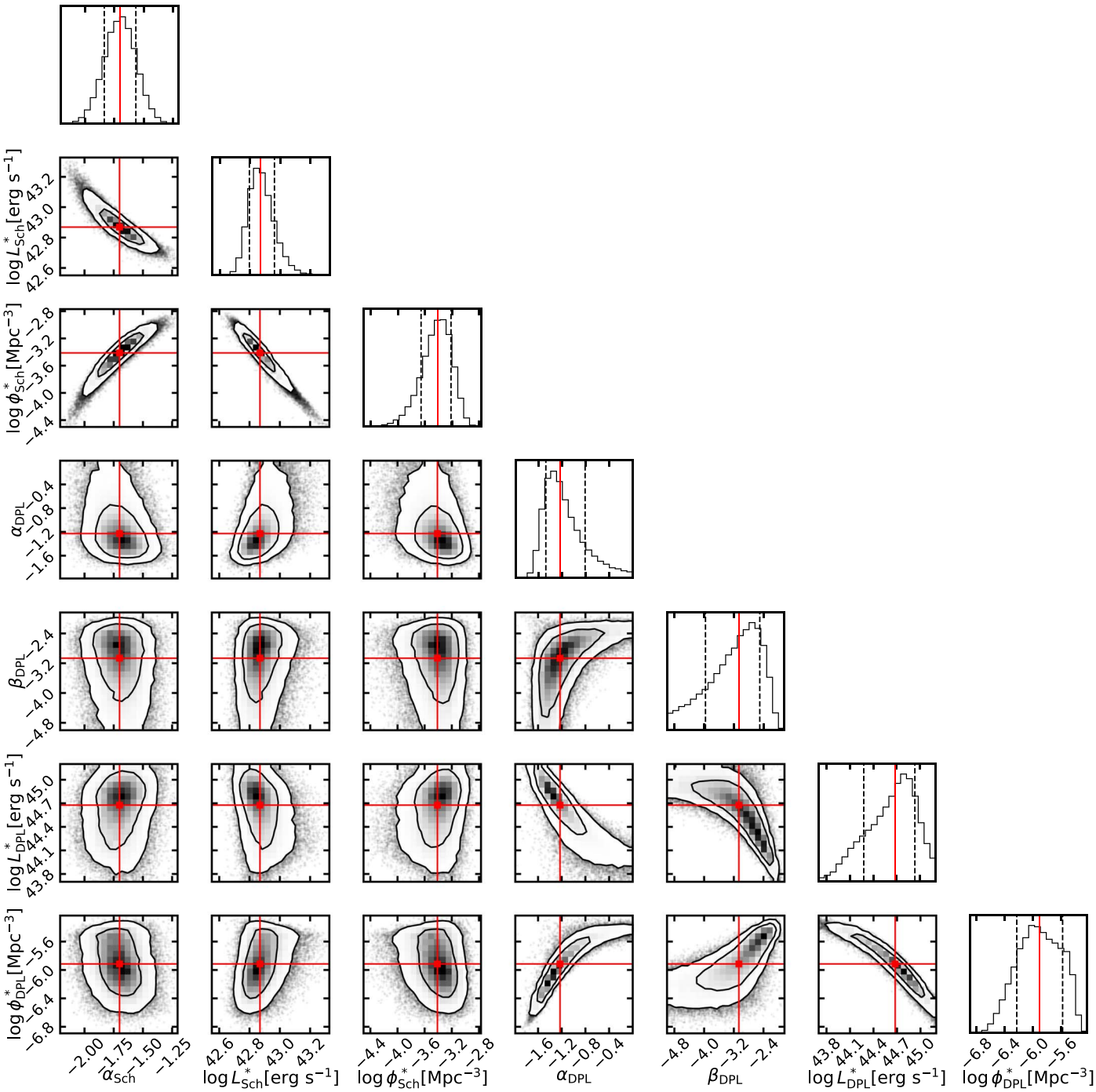

Figure 9. Error contours of our best-fit Lyα LF (model 1). The red squares denote the best-fit results of the parameters. The inner (outer) contour indicates the 68.3% (95.4%) confidence level.

$f_{\rm AGN,Ly\alpha}$ ($L_{\rm Ly\alpha}$) is Sobral et al. (2018b), based on 21 spectroscopically identified objects that include both type 1 and type 2 AGNs. At $\log L_{\rm Ly\alpha} \leqslant 43.5$ erg s^{-1}, our $f_{\rm AGN,Ly\alpha}$ are lower than their results. The small sample and inclusion of type 2 AGNs may explain the larger $f_{\rm AGN,Ly\alpha}$ from Sobral et al. (2018b).

Second, we estimate $f_{\rm AGN,Ly\alpha}$ with our best-fit Lyα LF, assuming that the faint Schechter component (bright DPL component) can well describe the Lyα LFs of SF galaxies (AGNs). A similar method was applied by Wold et al. (2017) and Spinoso et al. (2020) to derive $f_{\rm AGN,Ly\alpha}$ ($L_{\rm Ly\alpha}$). However, as mentioned in Spinoso et al. (2020), $f_{\rm AGN,Ly\alpha}$ ($L_{\rm Ly\alpha}$) estimated with this method only represents an illustrative result, given the strong assumption and high sensitivity to the determination of the faint Schechter component. We calculate $f_{\rm AGN,Ly\alpha}$ with

$$f_{\rm AGN,Ly\alpha}(\log L_{\rm Ly\alpha}) = \frac{\phi_{\rm bright}(\log L_{\rm Ly\alpha})}{\phi_{\rm bright}(\log L_{\rm Ly\alpha}) + \phi_{\rm faint}(\log L_{\rm Ly\alpha})}. \quad (13)$$

As shown in Figure 11, our $f_{\rm AGN,Ly\alpha}(L_{\rm Ly\alpha})$ estimated with Equation (13) agrees nicely with the ones derived with Equation (12). Comparing with the results from Spinoso et al. (2020) that are based on their bright AGN/QSO LFs and

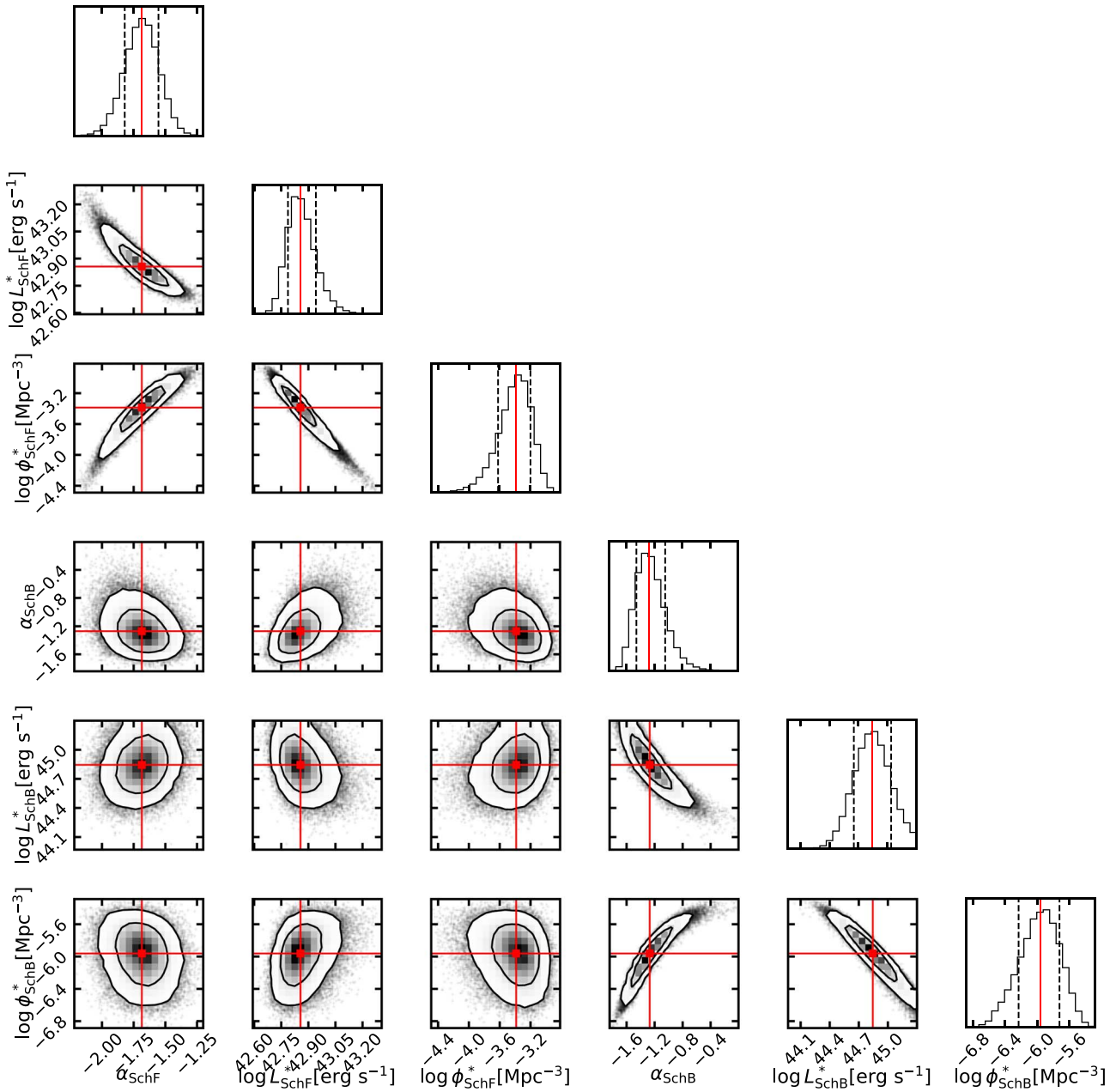

Figure 10. Same as Figure 9 but for model 2. The Schechter parameters of the faint and bright components are denoted with subscripts "SchF" and "SchB," respectively.

the faint SF galaxy LFs from Sobral et al. (2018a), our $f_{\rm AGN,Ly\alpha}$ ($L_{\rm Ly\alpha}$) has a similar increase and shifts toward brighter $L_{\rm Ly\alpha}$ by $\Delta \log L_{\rm Ly\alpha}/[\rm erg\ s^{-1}] \sim 0.3$–$0.5$. Wold et al. (2017) obtained an $f_{\rm AGN,Ly\alpha}$ ($L_{\rm Ly\alpha}$) similar to Spinoso et al. (2020) but with a flatter increase by fitting the observed LF from Konno et al. (2016) that has large scatters at the bright end. They also estimated the observed Lyα luminosity density contributed from SF galaxies ($\rho^{\rm obs}_{\rm Ly\alpha,SF}$) and AGNs ($\rho^{\rm obs}_{\rm Ly\alpha,AGN}$) to be $10^{39.7}$ and $10^{39.5}$ erg s^{-1} Mpc^{-3}, respectively, by integrating their best-fit Lyα LFs over the Lyα luminosity range of $\log L_{\rm Ly\alpha} = 41.41$–$44.4$ erg s^{-1}. They concluded that at $z = 2.2$, AGNs contribute ∼40% to the total observed Lyα luminosity density, which is consistent with their observational results at $z = 0.3$ and 0.9. We follow their method, calculating $\rho^{\rm obs}_{\rm Ly\alpha,SF}$ and $\rho^{\rm obs}_{\rm Ly\alpha,AGN}$ from our best-fit Lyα LF with

$$\rho^{\rm obs}_{\rm Ly\alpha,SF} = \int L_{\rm Ly\alpha}\,\phi_{\rm bright}(L_{\rm Ly\alpha})\,dL_{\rm Ly\alpha}, \quad (14)$$

$$\rho^{\rm obs}_{\rm Ly\alpha,AGN} = \int L_{\rm Ly\alpha}\,\phi_{\rm faint}(L_{\rm Ly\alpha})\,dL_{\rm Ly\alpha}. \quad (15)$$

We integrate Equations (14) and (15) over the same $L_{\rm Ly\alpha}$ range as mentioned in Wold et al. (2017), obtaining a $\rho^{\rm obs}_{\rm Ly\alpha,SF}$ ($\rho^{\rm obs}_{\rm Ly\alpha,AGN}$) value of $10^{39.7}$ ($10^{38.6}$) erg s^{-1} Mpc^{-3}. Despite the different shape of the best-fit Schechter function as presented in Figure 8, our $\rho^{\rm obs}_{\rm Ly\alpha,SF}$ is consistent with the result from Wold et al. (2017). Contrastingly, our $\rho^{\rm obs}_{\rm Ly\alpha,AGN}$ is ∼10 times lower, resulting in an AGN contribution of ∼8% to the total Lyα luminosity density at $z = 2.0$–3.2.

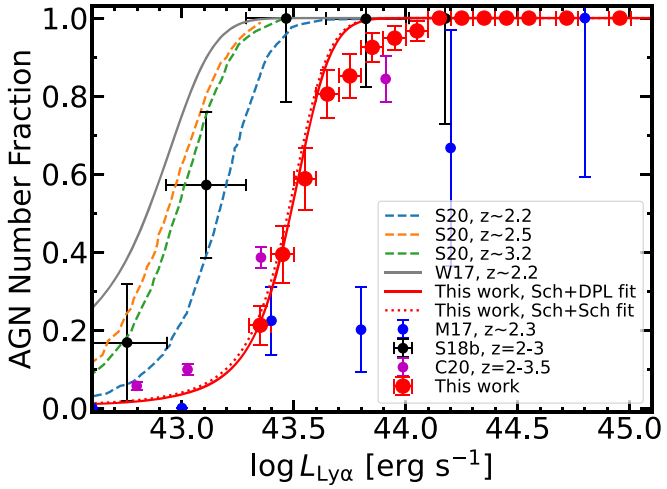

Figure 11. The AGN number fraction as a function of $\log L_{\mathrm{Ly}\alpha}$. Our results derived with Equation (12) are shown with red circles. The functional form of our $f_{\mathrm{AGN,Ly}\alpha}$ derived with Equation (13) using model 1 (2) is presented by the red solid (dashed) line. The other symbols represent previous measurements whose references are listed in the legend. M17: Matthee et al. (2017); W17: Wold et al. (2017); S18: Sobral et al. (2018b); C20: Calhau et al. (2020).

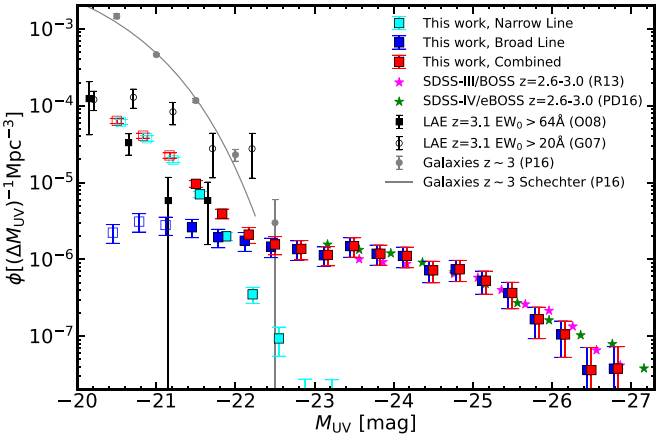

Figure 12. The UV LF of our NL (cyan squares), BL (blue squares), and C (red squares) LAEs. Data points that may be affected by incompleteness are marked with open squares. The magenta and green stars denote the QSO UV LF at $z \sim 2.8$ from SDSS-III (Ross et al. 2013; R13) and SDSS-IV (Palanque-Delabrouille et al. 2016; PD16), respectively. The black squares and black open circles indicate the LAE UV LFs from Ouchi et al. (2008; O08) and Gronwall et al. (2007; G07), respectively. We also show the UV LF of photometrically selected galaxies at $z \sim 3$ with the gray circles and solid line (Parsa et al. 2016; P16).

4.4. UV LF

We derive the UV LF of our LAE sample in the same manner as described in Section 4.3. We convert the r-band magnitude (r) of our LAEs to the absolute UV magnitude (M_{UV}) using the following relation:

$$M_{\mathrm{UV}} = r - 5\log\left(\frac{d_{\mathrm{L}}}{10\mathrm{pc}}\right) + 2.5\log(1+z) + K, \quad (16)$$

where d_{L} and z are the luminosity distance in parsecs and the redshift of our LAEs, respectively, determined by the Lyα emission lines in the HETDEX spectra. We set the k-correction term (K) to be zero according to our assumption of flat UV continua (Section 3.2). Figure 12 presents our UV LF at $-27 < M_{\mathrm{UV}} < -21$, where the completeness reaches 50%. At the bright end with $M_{\mathrm{UV}} < -22.5$, our results agree well with the SDSS QSO UV LF (Ross et al. 2013; Palanque-Delabrouille et al. 2016). Similar to our Lyα LF, the bright end of our UV LF is dominated by BL LAEs, indicating the presence of type 1 AGNs. At the faint end ($M_{\mathrm{UV}} > -21.5$), our UV LF enters the SF galaxy regime where previous results on the UV LFs of LAEs and photometrically selected galaxies are available. Our results are generally consistent with previous UV LFs of LAEs derived by Ouchi et al. (2008) and Gronwall et al. (2007). Our LAE sample may suffer incompleteness at $M_{\mathrm{UV}} > -21.3$ due to the detection limit of Lyα emission lines (Figure 3). As a result, only LAEs with the strongest Lyα emission lines are included in our sample. We denote our UV LF at $M_{\mathrm{UV}} > -21.3$ with open symbols.

We study the LAE number fraction (X_{LAE}) as a function of M_{UV} based on our LAE UV LF ($\phi_{\mathrm{UV,LAE}}$) and the best-fit UV LF of galaxies at $z \sim 3$ ($\phi_{\mathrm{UV,z=3}}$) derived by Parsa et al. (2016). They obtained their galaxy sample based on multiband photometry with the photometric redshift determined by SED fitting. By assuming that the galaxy sample of Parsa et al. (2016) is complete, we calculate X_{LAE} with

$$X_{\mathrm{LAE}}(M_{\mathrm{UV}}) = \frac{\phi_{\mathrm{UV,LAE}}(M_{\mathrm{UV}})}{\phi_{\mathrm{UV,z=3}}(M_{\mathrm{UV}})}. \quad (17)$$

In Figure 13, we present our results covering $-22.1 < M_{\mathrm{UV}} < -21.2$, where both our complete LAE UV LF and the galaxy UV LF are available. At $M_{\mathrm{UV}} < -21$, our results show that X_{LAE} increases toward brighter UV luminosity. Such a trend is mainly due to BL LAEs, whereas the number fraction of NL LAEs does not change at $-22.5 \lesssim M_{\mathrm{UV}} \lesssim -21$. We compare our results with the X_{LAE} values derived by two previous studies based on LBG samples at similar redshift, Stark et al. (2010) and Kusakabe et al. (2020), both of which focused on SF galaxies without AGNs. Stark et al. (2010) showed that X_{LAE} decreases with UV luminosity at $-22.5 < M_{\mathrm{UV}} < -18.5$. Their X_{LAE} at $M_{\mathrm{UV}} = -22$ is in agreement with our results derived from NL LAEs alone. Contrastingly, Kusakabe et al. (2020) found no UV luminosity dependence of X_{LAE} at $M_{\mathrm{UV}} \sim -20$ and -21, though their values are consistent with those in Stark et al. (2010) within the errors. Such a discrepancy may be caused by the increasing LBG selection bias toward faint M_{UV} (Kusakabe et al. 2020). Our results suggest that while the number fraction of SF-dominated LAEs has a tendency to decrease toward brighter UV luminosity, the number fraction of Lyα-emitting type 1 AGNs becomes dominant at $M_{\mathrm{UV}} \lesssim -21$ and increases toward brighter UV luminosity. This results in a turnaround of X_{LAE} at $M_{\mathrm{UV}} \sim -21$.

It should be noted that the UV LF of BL LAEs shown here is calculated from the total UV flux that includes both AGN and stellar components of host galaxies. In Section 6.2, we evaluate the contributions of UV continuum emission from AGNs and their host galaxies based on SED fitting results from Kakuma (2020) and discuss the redshift evolution of AGN activities.

Table 5
Emission Line Properties

Object	Emission Line	Wavelength (Å)	Flux (10^{-17} erg s^{-1} cm^{-2})	FWHM (km s^{-1})	Reduced χ^2
ID-4	C IV	5112.9	$37.83^{+1.06}_{-1.00}$	$4043.2^{+138.8}_{-136.4}$ ($5536.3^{+202.1}_{-185.8}$)[a]	1.157 (0.861)[b]
	(C III)	6287.7	$9.19^{+0.77}_{-0.75}$	$4268.0^{+373.7}_{-402.4}$	0.943
ID-5	C IV	4865.8	$2.50^{+0.35}_{-0.34}$	$1072.2^{+95.8}_{-104.4}$	1.043
	(C III)	5988.6	$2.50^{+0.57}_{-1.00}$	$2024.1^{+485.6}_{-1202.6}$	1.326

Notes.
[a] The number in parentheses indicates the FWHM of the broad component in the two-component Gaussian fit.
[b] The number in parentheses indicates the reduced χ^2 of the two-component Gaussian fit.

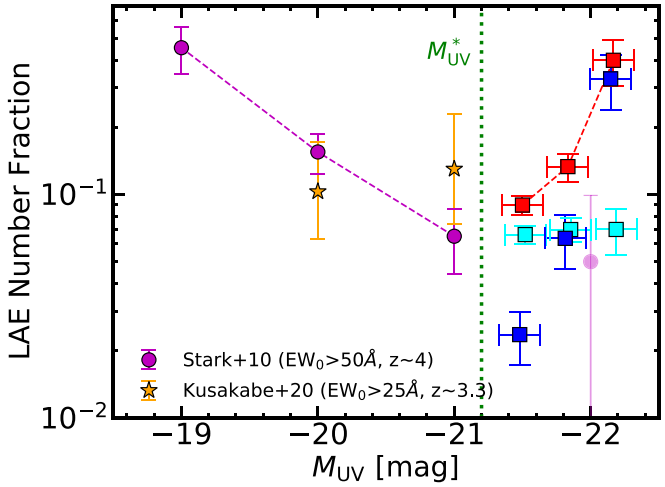

Figure 13. The X_{LAE} as a function of M_{UV}. The red, blue, and cyan squares denote our results derived from C, BL, and NL LAEs, respectively. The magenta circles and yellow stars represent the results from Stark et al. (2010) and Kusakabe et al. (2020), respectively. At M_{UV} fainter (brighter) than $M^*_{UV} \sim -21$, X_{LAE} increases (decreases) with M_{UV}.

5. Spectroscopic Properties of BL LAEs

In this section, we present the spectroscopic properties of the two faint BL LAEs with spectra, ID-4 and ID-5 (Table 3). We measure the central wavelengths, fluxes, and FWHMs of the C IV and [C III] emission lines (Figure 14) in the spectra of ID-4 and ID-5 with a best-fit Gaussian profile. We estimate the errors of fluxes and FWHMs by the Monte Carlo simulations. For each emission line, we make 1000 mock emission line spectra by adding noise to the observed line spectrum. The noise added to the observed line spectrum is generated following a Gaussian probability distribution whose standard deviation is the 1σ uncertainty in the observed line spectrum. The errors of the measured fluxes and FWHMs are defined as the 68% confidence intervals in the distributions of the fluxes and FWHMs in the mock emission line spectra. We measure the FWHMs of C IV and [C III], $\mathrm{FWHM_{CIV}}$ and $\mathrm{FWHM_{CIII]}}$, to be $4043.2^{+138.8}_{-136.4}$ ($1072.2^{+96.8}_{-104.4}$) and $4268.0^{+373.7}_{-402.4}$ ($2024.1^{+485.6}_{-1202.6}$) km s^{-1}, respectively, for ID-4 (ID-5). For the C IV emission line of ID-4, we find a broad component that cannot be well fitted with a single Gaussian profile. We fit the C IV emission line of ID-4 with a double Gaussian profile that consists of broad and narrow components, measuring the FWHM with the broad component of the double Gaussian profile. We obtain an $\mathrm{FWHM_{CIV}}$ of the broad component of $5536.3^{+202.1}_{-185.8}$ km s^{-1}. Table 5 summarizes the emission line properties of our objects.

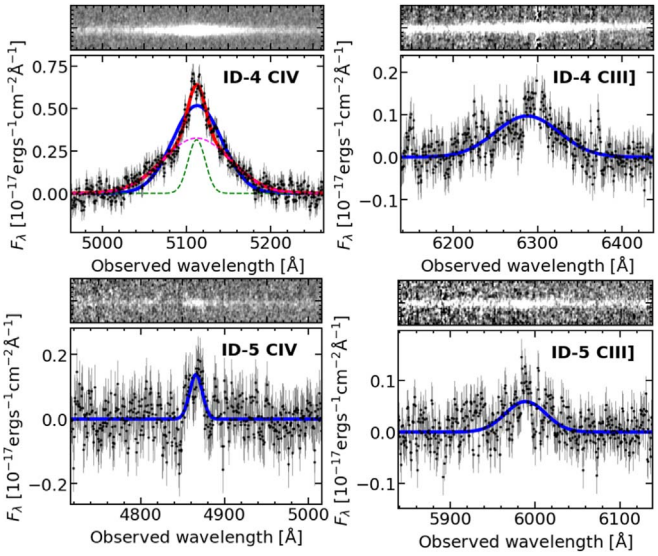

Figure 14. Emission line spectra of ID-4 and ID-5. At the top of each panel, we show the 2D spectrum. At the bottom of each panel, we present the 1D spectrum (black circles with errors) and the best-fit Gaussian profile (blue line). In the top right panel, we also show the best-fit double Gaussian profile (red line), as well as the broad (magenta dashed line) and narrow (green dashed line) components.

We use the scaling relations of Kim et al. (2018) with $\mathrm{FWHM_{CIV}}$ and the monochromatic continuum luminosity at rest frame 1350 Å (L_{1350}) to derive the BH masses M_{BH} of ID-4 and ID-5. We estimate L_{1350} by the log-linear extrapolation from the observed r- and i-band fluxes as listed in Table 3. The M_{BH} value is obtained with

$$\log\left(\frac{M_{BH}}{M_\odot}\right) = A + \log\left\{\left(\frac{L_{1350}}{10^{44}\ \mathrm{erg\ s^{-1}}}\right)^{\beta}\left(\frac{\mathrm{FWHM_{C\,IV}}}{1000\ \mathrm{km\ s^{-1}}}\right)^{\gamma}\right\}. \quad (18)$$

We adopt parameters (A, β, γ) of (6.7, 0.5, 2.0) that are taken from Kim et al. (2018). Our two faint BL LAEs, ID-4 and ID-5, have BH masses of $\log(M_{BH}/M_\odot) = 8.70^{+0.03}_{-0.03}$ and $6.85^{+0.08}_{-0.08}$, respectively.

From the M_{BH} values, we calculate the Eddington ratio (λ_{Edd}) of a BH, which is defined as

$$\lambda_{Edd} = L_{bol}/L_{Edd}, \quad (19)$$

where L_{bol} (L_{Edd}) is the bolometric (Eddington) luminosity of the BH. The L_{bol} are derived from L_{1350} with the bolometric

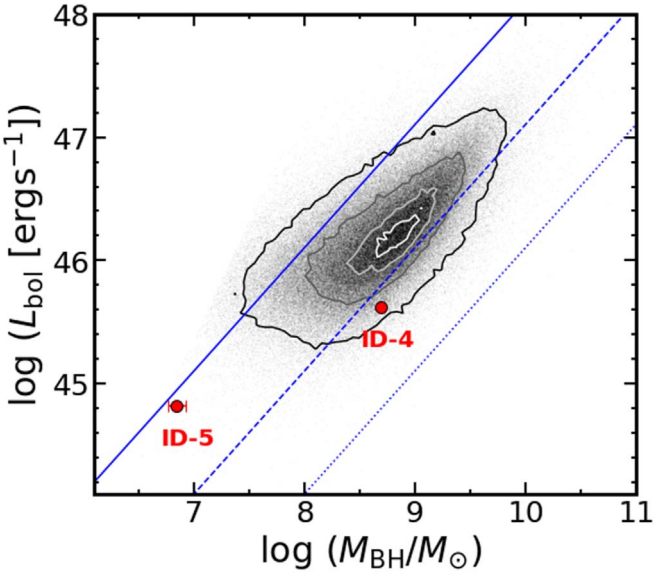

Figure 15. The M_{BH}–L_{bol} relation for ID-4 and ID-5. The red circles show our measurements. The gray data points and contours represent the results of $z = 2$–3.5 quasars in SDSS DR14 (Rakshit et al. 2020). The blue solid, dashed, and dotted lines correspond to the Eddington ratios $\lambda_{Edd} = 1$, 0.1, and 0.01, respectively.

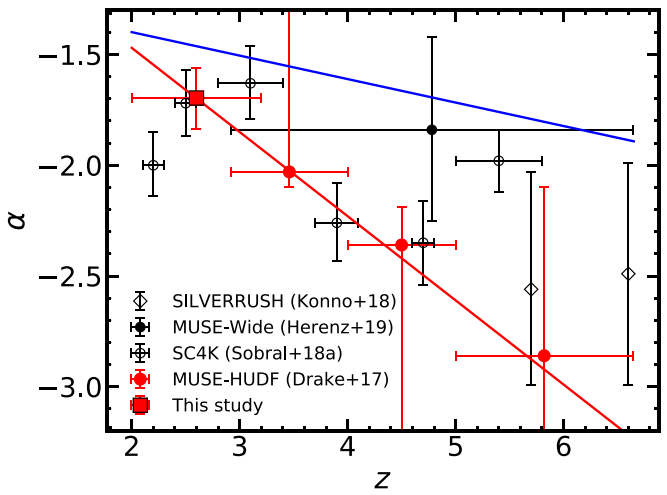

Figure 16. Evolution of the faint-end slope of the Lyα LF. Our result is denoted by the red square. The red circles, black filled circles, black open circles, and black open diamonds indicate the results from Drake et al. (2017), Herenz et al. (2019), Sobral et al. (2018a), and Konno et al. (2018), respectively. The error bars in the abscissa are the redshift ranges of the measurements. Our best-fit linear function is presented by the red line. The blue line shows the redshift evolution of the faint-end slope of the UV LF derived with photometrically selected galaxies (Parsa et al. 2016).

correction factor presented in Richards et al. (2006b) and Shen et al. (2011):

$$L_{bol} = 3.81 \times L_{1350}. \quad (20)$$

We derive the L_{bol} values of $10^{45.62}$ ($10^{44.82}$) erg s^{-1} for ID-4 (ID-5). The L_{Edd} is defined as

$$L_{Edd} = 1.26 \times 10^{38}\left(\frac{M_{BH}}{M_\odot}\right). \quad (21)$$

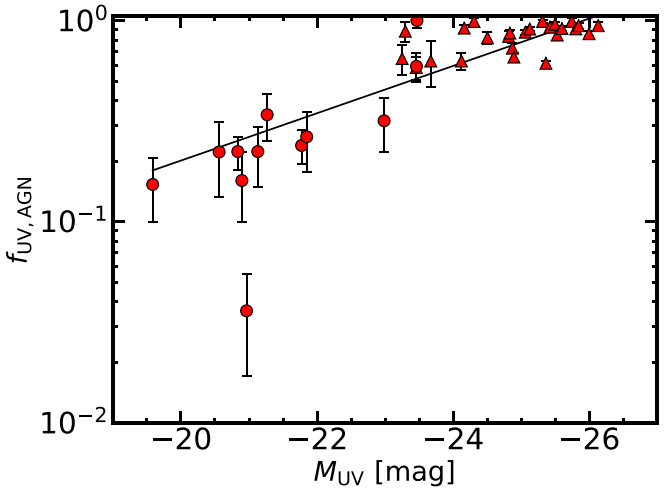

Figure 17. The M_{UV}–$f_{UV,AGN}$ relation derived by Kakuma (2020). The red circles (triangles) indicate type 1 AGNs selected from HETDEX (SDSS). Our best-fit linear function of $\log f_{UV,AGN} = -3.056 M_{UV} - 0.118$ is shown by the black solid line (see text).

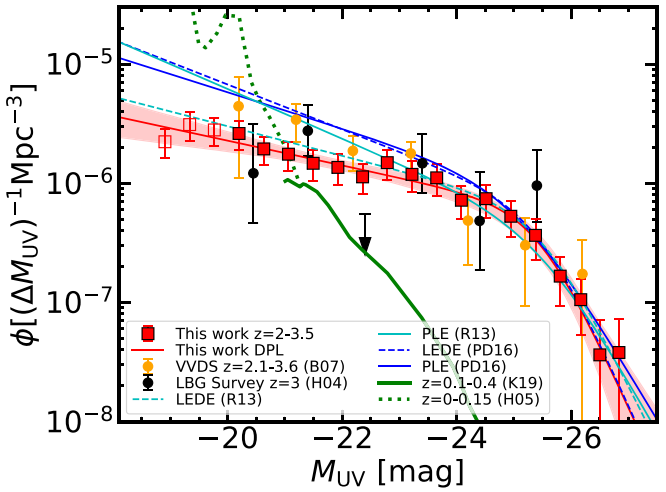

Figure 18. Type 1 AGN UV LF. Our results at $z = 2$–3.5 are presented by red squares. Similar to Figure 12, data points that may be affected by incompleteness are marked with open red squares. The yellow circles denote the AGN UV LF from the VVDS survey (Bongiorno et al. 2007; B07) at $z = 2.0$–3.5. The black circles indicate the AGN UV LF from the LBG survey (Hunt et al. 2004; H04) at $z \sim 3$. The cyan and blue lines are the predicted QSO UV LF at $z = 2.75$ from Ross et al. (2013; R13) and Palanque-Delabrouille et al. (2016; PD16), respectively, based on the PLE (solid) and LEDE (dashed) models. The green dashed and solid lines represent the UV LF of type 1 Seyfert galaxies at $0 < z < 0.15$ (Hao et al. 2005; H05) and the type 1 AGN UV LF at $0.1 < z < 0.4$ (Kulkarni et al. 2019; K19), respectively.

The Eddington ratios of ID-4 and ID-5 are $\lambda_{Edd} = 0.067^{+0.005}_{-0.004}$ and $0.746^{+0.111}_{-0.121}$, respectively. Figure 15 presents the M_{BH}–L_{bol} relation for ID-4 and ID-5.

6. Discussion

6.1. Faint-end Slope of Lyα LF

Although Gronke et al. (2015) predicted the evolution of the faint-end slope α_{Sch} of the Lyα LF based on a phenomenological model, such evolution has yet to be confirmed by observations. Combining our Lyα LF at $L_{Ly\alpha} \geqslant 10^{43.3}$ erg s^{-1} and the one derived by Cassata et al. (2011) at $L_{Ly\alpha} \leqslant 10^{43}$ erg s^{-1}, we

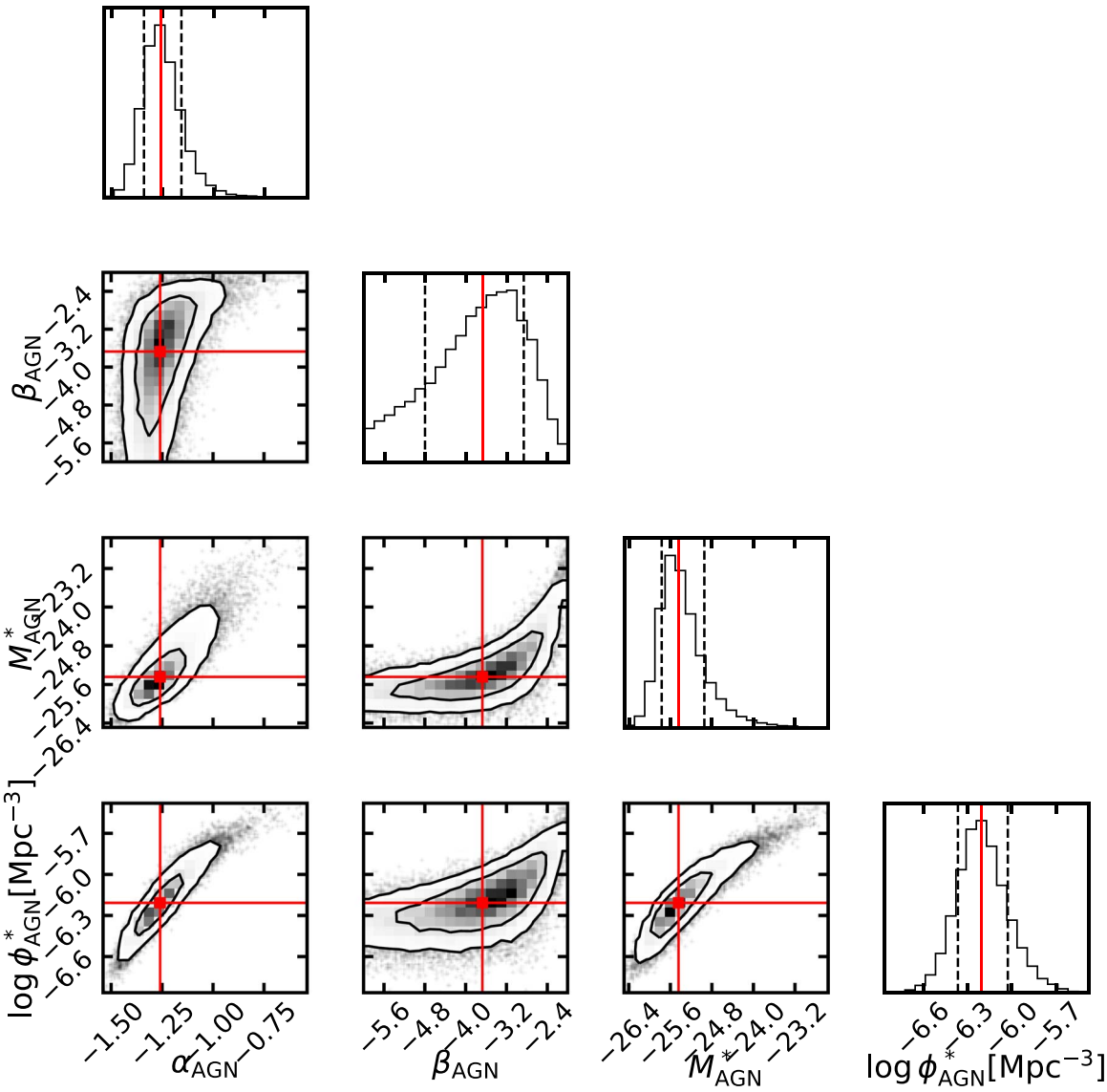

Figure 19. Same as Figure 9 but for the type 1 AGN UV LF.

reduce the degeneracy in L^*_{Sch} and α_{Sch} and obtain α_{Sch} by fitting the three Schechter parameters simultaneously. To study the evolution of the faint-end slope of the Lyα LF, we compare our result with α_{Sch} derived from previous photometric (Konno et al. 2018; Sobral et al. 2018a) and spectroscopic (Drake et al. 2017; Herenz et al. 2019) studies. We fit a linear relationship between α_{Sch} and z to the measurements from this work and Drake et al. (2017) in Figure 16. Our best-fit linear function has a slope of $-0.38^{+0.18}_{-0.26}$ and an intersection of $-0.71^{+0.86}_{-0.60}$. To evaluate the strength of the linear relation between α_{Sch} and z, we calculate the Pearson correlation coefficient r. We obtain the result of $r = -0.72$ with a p-value of 0.15, indicating a marginally significant trend of anticorrelation between α_{Sch} and z. Comparison between the α_{Sch}–z relation of the Lyα LF and that of the galaxy UV LF (Parsa et al. 2016) suggests that the α_{Sch} of the Lyα LF is steeper than that of the galaxy UV LF. Also, the evolution of the α_{Sch} of the Lyα LF is more rapid than that of the galaxy UV LF. The steepening of the α_{Sch} of the Lyα LF toward higher redshift is consistent with the observational results that dust attenuation of Lyα emission from SF galaxies decreases toward fainter UV luminosity (e.g., Ando et al. 2006; Ouchi et al. 2008) and higher redshift (e.g., Blanc et al. 2011; Hayes et al. 2011). Because SF galaxies become less dusty at higher redshift and lower mass, a larger fraction of faint LAEs are observed toward higher redshift. The increase in the fraction of faint LAEs may contribute to the rapid increase in Lyα escape fraction from $z \sim 2$ to 6 (Konno et al. 2016).

6.2. Type 1 AGN UV LF and the Evolution

As mentioned in Section 4.4, our UV LFs of BL LAEs are based on the total flux contributed from both the AGNs and stellar components of host galaxies. Here we refer to the type 1 AGN UV LF as the UV LF of BL LAEs with the flux contributed from the stellar components of galaxies removed. We derive the type 1 AGN UV LFs from UV LFs of BL LAEs using the AGN UV flux ratio ($f_{flux,AGN}$) that is defined as the ratio of flux contributed from AGNs to the total flux. Specifically, we calculate the $f_{flux,AGN}$ of our BL LAEs at each M_{UV} bin based on the results from Kakuma (2020). Kakuma (2020) obtained a sample of 37 type 1 AGNs at $z = 2$–3.5 using the same method as mentioned in Section 3.2.2 and conducted SED fitting on their sample with the Code Investigating GALaxy Emission (CIGALE; Boquien et al. 2019).

Their results are shown in Figure 17. Assuming a linear relation between $M_{\rm UV}$ and $\log f_{\rm flux,AGN}$, we obtain the following best-fit model by MCMC:

$$\log f_{\rm UV,AGN} = -3.056 M_{\rm UV} - 0.118. \quad (22)$$

We multiply the $M_{\rm UV}$ of the UV LF in Figure 12 by $f_{\rm flux,AGN}$, obtaining the type 1 AGN UV LFs as shown in Figure 18. Our results reach the very faint end of UV absolute magnitude at $M_{\rm UV} \sim -20$ and agree well with Bongiorno et al. (2007). Following the procedure mentioned in Section 4.3, we fit our type 1 AGN UV LF with the DPL,

$$\phi_{\rm AGN}(M_{\rm UV})dM_{\rm UV} = \frac{\phi^*_{\rm AGN}\, dM_{\rm UV}}{10^{(\alpha_{\rm AGN}+1)(M_{\rm UV}-M^*_{\rm AGN})} + 10^{(\beta_{\rm AGN}+1)(M_{\rm UV}-M^*_{\rm AGN})}}, \quad (23)$$

and obtain the best-fit parameters $\alpha_{\rm AGN} = -1.26^{+0.10}_{-0.08}$, $\beta_{\rm AGN} = -3.67^{+0.80}_{-1.13}$, $M^*_{\rm AGN} = -25.44^{+0.50}_{-0.33}$, and $\log \phi^*_{\rm AGN}[{\rm Mpc}^{-3}] = -6.21^{+0.18}_{-0.16}$. Our best-fit AGN UV LF and the posterior distributions of the parameters are shown in Figures 18 and 19, respectively. We compare our results with Ross et al. (2013) and Palanque-Delabrouille et al. (2016), who studied the QSO UV LF using the pure luminosity evolution (PLE) model and the luminosity evolution and density evolution (LEDE) model. As presented in Figure 18, our type 1 AGN UV LF is consistent with the LEDE model of Ross et al. (2013) at $z = 2.75$, suggesting that the AGN UV LF evolves in both luminosities and number densities. We also compare our LFs at $z = 2$–3 with those at low redshifts, the type 1 AGN UV LF at $0.1 < z < 0.4$ (Kulkarni et al. 2019), and the type 1 Seyfert UV LF at $0 < z < 0.15$ (Hao et al. 2005). In Figure 18, a strong evolution of type 1 AGN UV LFs is identified. At the bright end with $M_{\rm UV} < -22$, we reproduce previous results that show the decrease of number density toward low redshift. At the faint end with $M_{\rm UV} > -22$, our results show that the number density increases toward low redshift. Such a decrease (increase) of bright (faint) AGN number density toward low redshift can be interpreted as the AGN downsizing effect. First identified in X-ray studies (e.g., Hasinger 2008; Silverman et al. 2008), the AGN downsizing effect was observed in the UV LF only in the bright regime with $M_{\rm UV} \lesssim -21$ (e.g., Hopkins et al. 2007; Croom et al. 2009; Ikeda et al. 2012). Our results further support the AGN downsizing effect for the very faint AGNs with absolute UV magnitude down to $M_{\rm UV} \sim -20$.

The AGN downsizing effect may be connected with the quenching of massive galaxies that are observed in the local universe (e.g., Granato et al. 2004; Merloni 2004). Massive BHs, which reside in massive host galaxies, grow at a high accretion rate and make up the bright end of the AGN UV LFs at $z \sim 2$–3. Toward lower redshift, the intense AGN activity in massive galaxies may gradually dispel gas from dark matter halos, resulting in the halting of star formation in the host galaxies, as well as a decrease of the BH accretion rate. The AGNs become dimmer and populate the faint end of the UV LF. On the other hand, the moderate AGN feedback from less massive BHs would allow the host galaxies to keep their gas, supplying fuel to both star formation and BH accretion (e.g., Babić et al. 2007; Hirschmann et al. 2014).

To further investigate the redshift evolution of Lyα and UV LFs within $z \sim 2$–3, a larger sample of LAEs is needed. These analyses will be presented in our future studies that incorporate the forthcoming HETDEX data release.

7. Summary

We investigate the Lyα and UV LFs of LAEs at $z = 2$–3.5 that are obtained from the HETDEX spectroscopic survey. Our LAE sample includes 16,194 SF galaxies and 2126 type 1 AGNs with ${\rm EW}_0 > 20$ Å that are spectroscopically identified in a sky area of 11.4 deg^2. Our main results are summarized below.

We derive the Lyα LF of LAEs at $z = 2$–3.5 in the Lyα luminosity range of $43.3 < \log L_{\rm Ly\alpha}[{\rm erg\ s^{-1}}] < 45.5$. Our Ly$\alpha$ LF is consistent with those from previous studies. At $\log L_{\rm Ly\alpha}[{\rm erg\ s^{-1}}] > 43.5$, our Ly$\alpha$ LF shows a clear bright-end hump. This is the first confirmation of such a bright-end hump with spectroscopically identified LAE samples. We confirm that the bright-end hump can be fully explained by type 1 AGNs, which has been suggested in previous studies (e.g., Konno et al. 2016; Matthee et al. 2017; Sobral et al. 2018a; Calhau et al. 2020; Spinoso et al. 2020).

Combining our Lyα LF with the one derived by Cassata et al. (2011), we show that the Lyα LF at $z \sim 2$–3 can be fitted with the combination of the Schechter function and the DPL. Our Lyα LF provides strong constraints at the bright end, reducing the degeneracy of the faint-end slope $\alpha_{\rm Sch}$ and $L^*_{\rm Sch}$ by allowing all three Schechter parameters to be fitted simultaneously. From the Schechter component of our Lyα LF, we measure the faint-end slope to be $\alpha_{\rm Sch} = -1.70^{+0.13}_{-0.14}$ at $z = 2$–3.2. We investigate the redshift evolution of $\alpha_{\rm Sch}$ based on our measurement and those from previous studies. We find that there is a possible redshift evolution of $\alpha_{\rm Sch}$ over $z \sim 2$–6 with a correlation coefficient $r = -0.72$ at a confidence level of 85%. We obtain a linear relation $\alpha_{\rm Sch} = -0.38^{+0.18}_{-0.26}\, z - 0.71^{+0.86}_{-0.60}$ at $z \sim 2$–6. Comparing with the linear relation of the $\alpha_{\rm Sch}$ of the UV LF, we find that the $\alpha_{\rm Sch}$ of the Lyα LF may decrease more rapidly toward high redshift.

We derive the UV LF of LAEs at $z = 2$–3.5 in the range of $-27 < M_{\rm UV} < 20$, connecting the SF galaxy and AGN regimes. Our UV LFs are consistent with previous results of QSO UV LFs at $M_{\rm UV} < -23$ and LAE UV LFs at $M_{\rm UV} > -21.5$. Combining our results and the UV LF of galaxies at $z \sim 3$, we calculate the LAE number fraction as a function of $M_{\rm UV}$. Combining with previous measurements, we show that at $M_{\rm UV}$ fainter (brighter) than $M^*_{\rm UV} \sim -21$, $X_{\rm LAE}$ decreases (increases) with $M_{\rm UV}$.

We derive the type 1 AGN UV LF based on the UV LF of LAEs. Our type 1 AGN UV LF reaches a very faint absolute UV magnitude of $M_{\rm UV} \sim -20$ and agrees well with those from previous studies at similar redshift. Comparing with the results at lower redshifts, we find that the number density of faint ($M_{\rm UV} > -21$) AGNs increases from $z \sim 2$ to 0. Such a number density evolution is compatible with the AGN downsizing effect, which may have a close connection with the quenching of galaxy formation.

We thank the anonymous reviewer for the constructive comments that improved the quality of this work. Y.Z. thanks E. Komatsu for his help during the completion of this work. S.L.F. acknowledges support from the National Science Foundation through award AST-1908817. C.M.C. thanks the National Science Foundation for support through grants AST-1814034 and AST-2009577, the University of Texas at Austin

College of Natural Sciences, and the Research Corporation for Science Advancement from a 2019 Cottrell Scholar Award sponsored by IF/THEN, an initiative of Lyda Hill Philanthropies.

HETDEX is led by the University of Texas at Austin McDonald Observatory and Department of Astronomy with participation from the Ludwig-Maximilians-Universität München, Max-Planck-Institut für Extraterrestrische Physik (MPE), Leibniz-Institut für Astrophysik Potsdam (AIP), Texas A&M University, Pennsylvania State University, Institut für Astrophysik Göttingen, the University of Oxford, Max-Planck-Institut für Astrophysik (MPA), the University of Tokyo, and Missouri University of Science and Technology. In addition to institutional support, HETDEX is funded by the National Science Foundation (grant AST-0926815), the State of Texas, the US Air Force (AFRL FA9451-04-2- 0355), and generous support from private individuals and foundations. The observations were obtained with the Hobby–Eberly Telescope (HET), which is a joint project of the University of Texas at Austin, the Pennsylvania State University, Ludwig-Maximilians-Universität München, and Georg-August-Universität Göttingen. The HET is named in honor of its principal benefactors, William P. Hobby and Robert E. Eberly. VIRUS is a joint project of the University of Texas at Austin, Leibniz-Institut für Astrophysik Potsdam (AIP), Texas A&M University, Max-Planck-Institut für Extraterrestrische Physik (MPE), Ludwig-Maximilians-Universität München, the University of Oxford, Pennsylvania State University, Institut für Astrophysik Göttingen, and Max-Planck-Institut für Astrophysik (MPA). The Texas Advanced Computing Center (TACC) at the University of Texas at Austin provided high-performance computing, visualization, and storage resources that contributed to the research results reported within this paper.

The Institute for Gravitation and the Cosmos is supported by the Eberly College of Science and the Office of the Senior Vice President for Research at the Pennsylvania State University.

The Hyper Suprime-Cam (HSC) collaboration includes the astronomical communities of Japan and Taiwan and Princeton University. The HSC instrumentation and software were developed by the National Astronomical Observatory of Japan (NAOJ), the Kavli Institute for the Physics and Mathematics of the Universe (Kavli IPMU), the University of Tokyo, the High Energy Accelerator Research Organization (KEK), the Academia Sinica Institute for Astronomy and Astrophysics in Taiwan (ASIAA), and Princeton University. Funding was contributed by the FIRST program from the Japanese Cabinet Office, the Ministry of Education, Culture, Sports, Science and Technology (MEXT), the Japan Society for the Promotion of Science (JSPS), the Japan Science and Technology Agency (JST), the Toray Science Foundation, NAOJ, Kavli IPMU, KEK, ASIAA, and Princeton University.

This paper makes use of software developed for the Large Synoptic Survey Telescope. We thank the LSST Project for making their code available as free software at http://dm.lsst.org.

This research is based in part on data collected at Subaru Telescope, which is operated by the National Astronomical Observatory of Japan. We are honored and grateful for the opportunity to observe the universe from Maunakea, which has cultural, historical, and natural significance in Hawaii.

This paper is supported by World Premier International Research Center Initiative (WPI Initiative), MEXT, Japan, the joint research program of the Institute of Cosmic Ray Research (ICRR), the University of Tokyo, and KAKENHI (19H00697, 20H00180, and 21H04467) Grant-in-Aid for Scientific Research (A) through the Japan Society for the Promotion of Science.

ORCID iDs

Yechi Zhang https://orcid.org/0000-0003-3817-8739
Masami Ouchi https://orcid.org/0000-0002-1049-6658
Karl Gebhardt https://orcid.org/0000-0002-8433-8185
Erin Mentuch Cooper https://orcid.org/0000-0002-2307-0146
Chenxu Liu https://orcid.org/0000-0001-5561-2010
Dustin Davis https://orcid.org/0000-0002-8925-9769
Donghui Jeong https://orcid.org/0000-0002-8434-979X
Daniel J. Farrow https://orcid.org/0000-0003-2575-0652
Steven L. Finkelstein https://orcid.org/0000-0001-8519-1130
Eric Gawiser https://orcid.org/0000-0003-1530-8713
Gary J. Hill https://orcid.org/0000-0001-6717-7685
Yuichi Harikane https://orcid.org/0000-0002-6047-430X
Viviana Acquaviva https://orcid.org/0000-0002-6788-6315
Caitlin M. Casey https://orcid.org/0000-0002-0930-6466
Maximilian Fabricius https://orcid.org/0000-0002-7025-6058
Ulrich Hopp https://orcid.org/0000-0003-1008-225X
Matt J. Jarvis https://orcid.org/0000-0001-7039-9078
Martin Landriau https://orcid.org/0000-0003-1838-8528
Ken Mawatari https://orcid.org/0000-0003-4985-0201
Shiro Mukae https://orcid.org/0000-0003-3823-8279
Yoshiaki Ono https://orcid.org/0000-0001-9011-7605
Donald P. Schneider https://orcid.org/0000-0001-7240-7449

References

Aihara, H., AlSayyad, Y., Ando, M., et al. 2019, PASJ, 71, 114
Aihara, H., Arimoto, N., Armstrong, R., et al. 2018, PASJ, 70, S4
Ando, M., Ohta, K., Iwata, I., et al. 2006, ApJL, 645, L9
Babić, A., Miller, L., Jarvis, M. J., et al. 2007, A&A, 474, 755
Blanc, G. A., Adams, J. J., Gebhardt, K., et al. 2011, ApJ, 736, 31
Bongiorno, A., Zamorani, G., Gavignaud, I., et al. 2007, A&A, 472, 443
Boquien, M., Burgarella, D., Roehlly, Y., et al. 2019, A&A, 622, A103
Bosch, J., Armstrong, R., Bickerton, S., et al. 2018, PASJ, 70, S5
Bouwens, R. J., Illingworth, G. D., Oesch, P. A., et al. 2015, ApJ, 803, 34
Boyle, B. J., Shanks, T., Croom, S. M., et al. 2000, MNRAS, 317, 1014
Boyle, B. J., Shanks, T., & Peterson, B. A. 1988, MNRAS, 235, 935
Calhau, J., Sobral, D., Santos, S., et al. 2020, MNRAS, 493, 3341
Cassata, P., Le Fèvre, O., Garilli, B., et al. 2011, A&A, 525, A143
Croom, S. M., Richards, G. T., Shanks, T., et al. 2009, MNRAS, 399, 1755
Davis, M., Faber, S. M., Newman, J., et al. 2003, Proc. SPIE, 4834, 161
Dawson, S., Rhoads, J. E., Malhotra, S., et al. 2004, ApJ, 617, 707
Deharveng, J.-M., Small, T., Barlow, T. A., et al. 2008, ApJ, 680, 1072
Dijkstra, M., Haiman, Z., & Spaans, M. 2006, ApJ, 649, 14
Drake, A. B., Garel, T., Wisotzki, L., et al. 2017, A&A, 608, A6
Eddington, A. S. 1913, MNRAS, 73, 359
Fabian, A. C. 2012, ARA&A, 50, 455
Farrow, D. J., Sánchez, A. G., Ciardullo, R., et al. 2021, MNRAS, 507, 3187
Felten, J. E. 1976, ApJ, 207, 700
Finkelstein, S. L., Rhoads, J. E., Malhotra, S., & Grogin, N. 2009, ApJ, 691, 465
Finkelstein, S. L., Rhoads, J. E., Malhotra, S., Grogin, N., & Wang, J. 2008, ApJ, 678, 655
Finkelstein, S. L., Rhoads, J. E., Malhotra, S., Pirzkal, N., & Wang, J. 2007, ApJ, 660, 1023
Finkelstein, S. L., Ryan, R. E. J., Papovich, C., et al. 2015, ApJ, 810, 71
Foreman-Mackey, D., Hogg, D. W., Lang, D., & Goodman, J. 2013, PASP, 125, 306
Gawiser, E., van Dokkum, P. G., Gronwall, C., et al. 2006, ApJL, 642, L13

Granato, G. L., De Zotti, G., Silva, L., Bressan, A., & Danese, L. 2004, ApJ, 600, 580
Gronke, M., Dijkstra, M., Trenti, M., & Wyithe, S. 2015, MNRAS, 449, 1284
Gronwall, C., Ciardullo, R., Hickey, T., et al. 2007, ApJ, 667, 79
Hao, L., Strauss, M. A., Fan, X., et al. 2005, AJ, 129, 1795
Harikane, Y., Ouchi, M., Shibuya, T., et al. 2018, ApJ, 859, 84
Hasinger, G. 2008, A&A, 490, 905
Hayes, M., Schaerer, D., Östlin, G., et al. 2011, ApJ, 730, 8
Herenz, E. C., Wisotzki, L., Saust, R., et al. 2019, A&A, 621, A107
Hill, G. J. 2014, AdOT, 3, 265
Hill, G. J., Drory, N., Good, J. M., et al. 2018b, Proc. SPIE, 10700, 107000P
Hill, G. J., Gebhardt, K., Komatsu, E., et al. 2008, in ASP Conf. Ser. 399, The Hobby-Eberly Telescope Dark Energy Experiment (HETDEX): Description and Early Pilot Survey Results, ed. T. Kodama, T. Yamada, & K. Aoki (San Francisco, CA: ASP), 115
Hill, G. J., Kelz, A., Lee, H., et al. 2018a, Proc. SPIE, 10702, 107021K
Hirschmann, M., Dolag, K., Saro, A., et al. 2014, MNRAS, 442, 2304
Hopkins, P. F., Richards, G. T., & Hernquist, L. 2007, ApJ, 654, 731
Hu, E. M., Cowie, L. L., Barger, A. J., et al. 2010, ApJ, 725, 394
Hunt, M. P., Steidel, C. C., Adelberger, K. L., & Shapley, A. E. 2004, ApJ, 605, 625
Ikeda, H., Nagao, T., Matsuoka, K., et al. 2012, ApJ, 756, 160
Itoh, R., Ouchi, M., Zhang, H., et al. 2018, ApJ, 867, 46
Kakuma, R. 2020, Master's thesis, The Univ. of Tokyo, Tokyo, Japan
Kashikawa, N., Nagao, T., Toshikawa, J., et al. 2012, ApJ, 761, 85
Kashikawa, N., Shimasaku, K., Malkan, M. A., et al. 2006, ApJ, 648, 7
Kelz, A., Jahn, T., Haynes, D., et al. 2014, Proc. SPIE, 9147, 914775
Kim, Y., Im, M., Jeon, Y., et al. 2018, ApJ, 855, 138
Koekemoer, A. M., Aussel, H., Calzetti, D., et al. 2007, ApJS, 172, 196
Konno, A., Ouchi, M., Nakajima, K., et al. 2016, ApJ, 823, 20
Konno, A., Ouchi, M., Shibuya, T., et al. 2018, PASJ, 70, S16
Kriek, M., Shapley, A. E., Reddy, N. A., et al. 2015, ApJS, 218, 15
Kulkarni, G., Worseck, G., & Hennawi, J. F. 2019, MNRAS, 488, 1035
Kusakabe, H., Blaizot, J., Garel, T., et al. 2020, A&A, 638, A12
Laigle, C., McCracken, H. J., Ilbert, O., et al. 2016, ApJS, 224, 24
Leung, A. S., Acquaviva, V., Gawiser, E., et al. 2017, ApJ, 843, 130
Lusso, E., Worseck, G., Hennawi, J. F., et al. 2015, MNRAS, 449, 4204
Malhotra, S., & Rhoads, J. E. 2004, ApJL, 617, L5
Massey, R., Stoughton, C., Leauthaud, A., et al. 2010, MNRAS, 401, 371
Matthee, J., Sobral, D., Best, P., et al. 2017, MNRAS, 471, 629
Matthee, J., Sobral, D., Gronke, M., et al. 2018, A&A, 619, A136
Merloni, A. 2004, MNRAS, 353, 1035
Merloni, A., & Heinz, S. 2013, in Evolution of Active Galactic Nuclei, ed. T. D. Oswalt & W. C. Keel, Vol. 6 (Dordrecht: Springer), 503
Moffat, A. F. J. 1969, A&A, 3, 455
Nagao, T., Motohara, K., Maiolino, R., et al. 2005, ApJL, 631, L5
Netzer, H. 1990, in Active Galactic Nuclei, ed. R. Blandford et al. (Berlin: Springer), 57
Oke, J. B. 1974, ApJS, 27, 21
Ono, Y., Ouchi, M., Shimasaku, K., et al. 2010a, ApJ, 724, 1524
Ono, Y., Ouchi, M., Shimasaku, K., et al. 2010b, MNRAS, 402, 1580
Ouchi, M., Ono, Y., & Shibuya, T. 2020, ARA&A, 58, 617
Ouchi, M., Shimasaku, K., Akiyama, M., et al. 2008, ApJS, 176, 301
Ouchi, M., Shimasaku, K., Furusawa, H., et al. 2010, ApJ, 723, 869
Palanque-Delabrouille, N., Magneville, C., Yèche, C., et al. 2016, A&A, 587, A41
Pâris, I., Petitjean, P., Aubourg, É., et al. 2018, A&A, 613, A51
Parsa, S., Dunlop, J. S., McLure, R. J., & Mortlock, A. 2016, MNRAS, 456, 3194
Pei, Y. C. 1995, ApJ, 438, 623
Pentericci, L., Grazian, A., Fontana, A., et al. 2009, A&A, 494, 553
Rakshit, S., Stalin, C. S., & Kotilainen, J. 2020, ApJS, 249, 17
Ramsey, L. W., Sebring, T. A., & Sneden, C. A. 1994, Proc. SPIE, 2199, 31
Rhoads, J. E., Malhotra, S., Dey, A., et al. 2000, ApJL, 545, L85
Richards, G. T., Lacy, M., Storrie-Lombardi, L. J., et al. 2006b, ApJS, 166, 470
Richards, G. T., Strauss, M. A., Fan, X., et al. 2006a, AJ, 131, 2766
Ross, N. P., McGreer, I. D., White, M., et al. 2013, ApJ, 773, 14
Sakai, N. 2021, Master's thesis, The Univ. of Tokyo, Tokyo, Japan
Schechter, P. 1976, ApJ, 203, 297
Schmidt, M. 1968, ApJ, 151, 393
Schwarz, G. 1978, AnSta, 6, 461
Shen, Y., Richards, G. T., Strauss, M. A., et al. 2011, ApJS, 194, 45
Silverman, J. D., Green, P. J., Barkhouse, W. A., et al. 2008, ApJ, 679, 118
Sobral, D., Matthee, J., Best, P., et al. 2017, MNRAS, 466, 1242
Sobral, D., Matthee, J., Darvish, B., et al. 2018b, MNRAS, 477, 2817
Sobral, D., Santos, S., Matthee, J., et al. 2018a, MNRAS, 476, 4725
Spinoso, D., Orsi, A., López-Sanjuan, C., et al. 2020, A&A, 643, A149
Stark, D. P., Ellis, R. S., Chiu, K., Ouchi, M., & Bunker, A. 2010, MNRAS, 408, 1628
Stevans, M. L., Finkelstein, S. L., Wold, I., et al. 2018, ApJ, 863, 63
Tasca, L. A. M., Le Fèvre, O., Ribeiro, B., et al. 2017, A&A, 600, A110
Tilvi, V., Malhotra, S., Rhoads, J. E., et al. 2020, ApJL, 891, L10
Tody, D. 1986, Proc. SPIE, 627, 733
Trujillo, I., Aguerri, J. A. L., Cepa, J., & Gutiérrez, C. M. 2001, MNRAS, 328, 977
Verhamme, A., Garel, T., Ventou, E., et al. 2018, MNRAS, 478, L60
Wold, I. G. B., Finkelstein, S. L., Barger, A. J., Cowie, L. L., & Rosenwasser, B. 2017, ApJ, 848, 108
Zheng, Z.-Y., Finkelstein, S. L., Finkelstein, K., et al. 2013, MNRAS, 431, 3589
Zheng, Z.-Y., Wang, J., Rhoads, J., et al. 2017, ApJL, 842, L22